Designing a Calibration System for the Outer Detector of the nEXO Experiment

Samin Majidi

A THESIS SUBMITTED IN PARTIAL FULFILLMENT

OF THE REQUIREMENTS FOR THE DEGREE OF

Master of Science

Department of Physics
McGill University
Montréal, Québec, Canada

August 2023

Abstract

One of the fundamental questions in physics revolves around the existence of matter in our universe. To address this question, various approaches have been proposed. One avenue involves investigating the nature of neutrinos, specifically whether they are Dirac or Majorana particles. This investigation focuses on a specific process known as neutrinoless double beta ($0\nu\beta\beta$) decay, in which two neutrons transform into two protons and two electrons without any neutrinos in the final state. Detecting such a decay would not only indicate lepton number violation but also validate the Majorana nature of neutrinos.

A proposed experiment named the nEXO experiment aims to search for this rare decay with a projected half-life sensitivity of 10^{28} years at the 90% Confidence Level, or 10^{18} times the age of the universe. nEXO will accumulate data using 5 tonnes of liquid xenon enriched to 90% in the isotope ^{136}Xe. However, the potential signal from this decay is extremely rare and susceptible to external backgrounds. As a result, a robust shielding strategy against radioactive backgrounds is crucial, which involves implementing multiple layers. One of these layers is a water tank measuring 12.8 meters in height and 12.3 meters in diameter, containing 1.5 kilotonnes of ultra-pure water. In the proposed configuration an array of 125 photomultiplier tubes (PMTs) is deployed in the tank to serve as a muon veto detector. This is referred to as the Outer Detector.

Ensuring the operational integrity of the PMTs and monitoring water quality requires designing a calibration system for the Outer Detector. This calibration system utilizes laser sources to emit light into the water tank, directing it towards five diffuser balls positioned within the tank through optical fibres. This approach guarantees accurate calibration and continuous monitoring of the Outer Detector's performance.

Abrégé

Une des questions fondamentales en physique discute de l'existence de la matière dans notre Univers. Plusieurs voies ont été proposés pour aborder cette question. Une approche possible est d'examiner la nature des neutrinos, spécifiquement s'ils sont des particles Dirac ou Majorana. Cette recherche est axée sur le processus de double désintégration beta sans émission de neutrinos ($0\nu\beta\beta$), au cours duquel deux neutrons se transforment en deux protons et deux electrons, sans aucun neutrino dans l'état final. La détection de cette désintégration indiquerait l'infraction du nombre de lepton et confirmerait la nature Majorana des neutrinos.

Une expérience proposée, le nEXO experiment, vise à rechercher de cette désintégration rare. nEXO vise une sensibilité de demi-vie de 10^{28} années avec un niveau de confiance de 90%, ou 10^{18} fois l'age de l'univers. nEXO va prendre des données avec 5 tonnes de Xenon liquide enrichi de l'isotope ^{136}Xe. Toutefois, le signal de cette désintégration est extrêmement faible et susceptible au rayonnement externe. Il est donc impératif d'avoir une stratégie de blindage robuste, c'est-à-dire plusieurs couches. Une de ces couches est un réservoir d'eau qui fait 12.8 m de hauteur et 12.3 m de diamètre, et qui contient 1.5 kilotonnes d'eau désionisée ultra-pure. Cette couche se nomme le Outer Detector. Dans la configuration proposée du Outer Detector, 125 tubes photomultiplicateurs (PMTs) sont étalées en tant que détecteur veto de muons.

La conception d'un système de calibration pour le Outer Detector est nécéssaire pour assurer l'intégrité opérationnelle des PMTs et contrôler la qualité de l'eau. Ce système de calibration utilize des sources de laser pour émettre de la lumière dans le réservoir d'eau, et la diriger à travers des fibres optiques vers cinq balles de diffusion positionnées à travers le réservoir. Cette approche assure une calibration précise et un contrôle continu de la performance du Outer Detector.

Acknowledgements

I am profoundly grateful to Prof. Thomas Brunner and Dr. Erica Caden, my supervisors, for their unyielding support. Their scientific guidance and unwavering mentorship have not only shaped my research but have also enriched my personal growth. Their encouragement has been the driving force behind my pursuit.

My heartfelt appreciation extends to the entire Brunner Neutrino Group for their collective wisdom and camaraderie. The willingness of each member to share knowledge and address my questions has been a beacon of support. Soud Al Kharusi's generous assistance, particularly in matters concerning the Outer Detector and Chroma simulations, has been indispensable to my progress.

The nEXO Collaboration, especially the Outer Detector Team, holds a special place in my journey. Their advice and insights have illuminated the complexities of the Outer Detector realm and significantly elevated my understanding. Liam Retty's exceptional work in designing the Outer Detector using Fusion 360 has been transformative.

My gratitude extends beyond academia to encompass my family. To my mother and sister, unwavering pillars of support, I owe the beginning of this journey. Their encouragement and belief in me have formed the foundation upon which I've built my aspirations.

To all those mentioned and those who have quietly played a part, my sincere thanks. Your support, in its many forms, has been the driving force behind my progress.

Contribution of Authors

I wrote all the chapters of the thesis, covering conceptualization, literature review, methodology, analysis, and conclusion. Sandhya Rottoo contributed by translating the abstract of the thesis into French.

The Chroma simulation framework, initially developed by Stanley Seibert and Anthony LaTorre, formed the basis for this study. Soud Al Kharusi and David Gallacher worked together with me to modify the Chroma simulation code to reflect the calibration system requirements. Liam Retty played a crucial role in preparing the Outer Detector geometry for nEXO and ensuring its proper representation in this study's simulations.

Contents

Chapter 1

Why Do Neutrinos Matter?

Neutrinoless double beta ($0\nu\beta\beta$) decay is a hypothetical decay process that may occur in specific atomic nuclei. This process involves the simultaneous decay of two neutrons into two protons and two electrons however with no neutrinos existing in the final state. Observing $0\nu\beta\beta$ would provide evidence for the Majorana nature of neutrinos since the requirement for such a decay is for the neutrinos to be their own antiparticles. The search for $0\nu\beta\beta$ in ^{136}Xe is one of the active areas probing for physics beyond the Standard Model of particle physics. For that, ton-scale experiments with specific technologies and layers of shielding from various sources of background radiation are needed. The nEXO experiment is a proposed detector search for this rare decay with a half-life sensitivity beyond 10^{28} years.

1.1 Introduction

1.1.1 The Way to the Big Question

Cosmological observations suggest that we live in a universe that has been created in the Big Bang. The most reliable theory for our universe's origin is that it has been expanding and cooling ever since it emerged from a single point of immense heat and density [1]. Matter and antimatter were produced in about equal amounts when the universe formed. The interaction between matter and antimatter leads to the annihilation into energy in the form of photons. However, for some reason, more matter was produced leading to a world

that is matter dominated. One approach to addressing this question involves determining the nature of neutrinos as either Dirac or Majorana particles.

Particles have an antimatter counterpart, an object with the same mass but the opposite charge and other quantum numbers [2]. The equation that first predicted antimatter particles in 1928 was written by Paul Dirac, while the discovery of antimatter was made by Carl Anderson in 1932 by observation of the positron [3]. According to Dirac's prediction, matter and antimatter should have another opposite attribute in addition to carrying opposite charges, called chirality. Chirality itself is described by another parameter, helicity. If a particle's spin and motion are in the same direction, its helicity is positive (right-handed). In contrast, a particle with the opposite direction of spin and motion has negative helicity (left-handed). The chirality of an object refers to the way the particle gets transformed into a right-handed or left-handed representation of the Poincaré group. In special relativity, the laws of physics are invariant under the Poincaré group transformations, meaning they remain the same in all inertial reference frames [4].

For massless particles, chirality and helicity are the same. Regardless of the observer's point of view, the spin of a massless particle is in the same direction along its axis of motion. Nevertheless, in the case of massive particles, the observer can change to a reference frame moving faster than the spinning particle. In this case, the particle will appear to be moving backward, and its apparent helicity or chirality will be reversed [4].

Accordingly, matter and antimatter are distinguishable whether by their charge (charged particles) or their chirality (massive particles). Those particles that differ from their antiparticles are called Dirac particles, while those that can act as their own antiparticles are known as Majorana particles.

Dirac's equation established that neutrinos and antineutrinos are different particles. As a result, neutrinos with left- and right-handed chirality and antineutrinos with left- and right-handed chirality were possible. But in the Standard Model of particle physics neutrinos were assumed to be massless. Hence, only left-handed neutrinos and right-handed antineutrinos were allowed to exist. It was Ettore Majorana who proposed in 1937 that neutrinos with mass can turn into their antiparticles and back again [4]. By describing neutrinos with the Majorana equation, they could turn into antineutrinos and then back into neutrinos again

if they happened to have mass. The mass of neutrinos remained a mystery until 1998, when it was discovered that they do indeed have tiny masses by the Super-Kamiokande and SNO experiments [5]. This achievement won the 2015 Physics Nobel Prize [6].

The critical parameter which pushed neutrino studies ahead was the lepton number. Lepton number refers to a quantum number representing the difference between the number of leptons and antileptons in an interaction of elementary particles. Neutrinos are lepton, so any neutrino has lepton number equal to 1, while antineutrinos have a lepton number equal to -1. In nature, the lepton number is conserved in weak interactions. This lepton number conservation makes the electrically neutral leptons distinguishable from their antiparticles. If neutrinos are recognizable from antineutrinos, the identification will be the lepton number value. In this case, neutrinos are described as Dirac neutrinos. However, the lepton number might not be conserved in nature. Thus, there is nothing to distinguish a neutrino from its antineutrino and it will be a Majorana neutrino [7].

In general, there exist two scenarios regarding the nature of neutrinos:

— Neutrinos follow Dirac's equation; thus, they are different from their antineutrinos. As a result, there must be two additional states (right-handed neutions and left-handed antineutrinos) which are missing, and physicists have yet to spot them.

— Neutrinos follow Majorana prediction; where, neutrinos and antineutrinos are identical. Spotting evidence of neutrinoless double beta decay would determine the Majorana nature of neutrinos.

1.1.2 Neutrinos

Smaller in mass than an electron by at least six orders of magnitude, neutrinos are one of the most mysterious particle in the Standard Model [8]. Of all the mass-containing subatomic particles, they are the lightest. They are the second most abundant particle after photons and the most abundant massive particle in the universe. Neutrinos, same as electrons, belong to the family of leptons. Particles in this family do only interact with electroweak force and gravity [9–11].

Neutrinos are electrically neutral which means they do not directly interact with the electromagnetic force. Because of the neutrino's remarkably low mass, the gravitational in-

teraction is relatively weak and neutrinos do not participate in the strong interaction. Among the four fundamental forces, the weak interaction possesses the shortest range. Consequently, the influence of the weak force becomes prominent solely within very short distances. Based on this fact, neutrinos can travel very long distances without interacting with materials, making them difficult to detect and study. At the same time, the weak force interacts with left-handed particles and right-handed antiparticles, which means the weak force is handed and only couples to particles with a specific chirality (i.e., left-handed) and their corresponding antiparticles with opposite chirality (i.e., right-handed). This property is related to the fact that the weak force is transmitted by the exchange of W and Z bosons, which have a specific spin orientation that couples preferentially to left-handed particles. Treating left-handed and right-handed particles differently by the weak force arises from the fact that it violates the parity symmetry [9–11].

Neutrinos come in three flavours: the electron neutrino (ν_e), the muon neutrino (ν_μ) and the tau neutrino (ν_τ). Each flavour is associated with the correspondingly named charged lepton. As a neutrino interacts, its partner particle typically is created, allowing us to identify the flavour of the interacting neutrino. The neutrino itself has never been directly observed; other particles created when a neutrino interacts in a detector are signs of neutrinos [12].

The Standard Model of particle physics, a highly successful framework that describes all the known fundamental particles and their interactions with fundamental forces (the electromagnetic, weak and strong forces) except for gravity, assumes neutrinos to be massless because they are described as left-handed chiral fermions, which means they only interact with the weak force in a way that is invariant under a symmetry known as the chiral symmetry. This symmetry prohibits the introduction of mass terms for neutrinos [13].

Experiments in which neutrinos change their flavour proved that neutrinos have mass. Although the absolute mass of the neutrino is still unknown, it has been determined that the masses of three known types of neutrinos are different, and the sum of all three of those types is still less than one millionth the mass of an electron. Also, it is known that the three masses do not uniquely correspond to the three flavours: A neutrino created with a particular flavour is a specific mixture of all three mass states (a quantum superposition). As a result, neutrinos oscillate between their different flavours. For example, an electron

neutrino produced in a beta decay reaction may interact as a muon or tau neutrino. This is called neutrino oscillations [12].

As mentioned previously, in the Standard Model, neutrinos are assumed to be massless; therefore, neutrino mass is a parameter beyond the Standard Model. The mass term of neutrinos cannot be added to the Standard Model since it leads to other problems. One of the issues that needs to be better understood is whether the origin of neutrino mass is the same as the other fundamental particles'. The charged leptons and quarks acquire their masses through interactions with the Higgs boson, but that is not necessarily the case for neutrinos [14].

The existence of neutrinos was predicted in 1930, but it took 26 years for experiments to be able to discover them [15]. Today, scientists are trying to determine the different characteristics of neutrinos. Neutrino mass, its interaction with matter, and its possibility to be a Majorana particle are topics that need more study and research. The peculiarity of neutrinos might hold the answer to one of the fundamental questions about the world; what happened to all the antimatter following the Big Bang.

Indirect neutrino mass measurement via cosmological observables, direct neutrino mass measurement based on the kinematics of single beta decay and the search for neutrinoless double beta decay are currently three primary approaches for studying neutrinos [8]. In general, neutrinos could provide a tool for studying physics beyond the Standard Model as well as participating in a broad range of physics like the supernovae explosions, the early universe, and the interior of the Earth.

1.1.3 Double Beta Decay

1.1.3.1 Ordinary Double Beta Decay

A typical candidate for double beta decay is an even-even nucleus with atomic numbers (Z) and mass numbers (A), where the pairing forces render it more tightly bound than its neighboring nucleus with (Z+1, A) but less bound than the (Z+2, A). When examining isotopes with the same atomic number, their masses around the stable isotope can be approximated using a parabolic curve, as illustrated in Figure 1.1. Isotopes on the left side of

this curve decay through β^- decay, while those on the right undergo β^+ decay and electron capture. In cases involving odd-odd and even-even nuclei, where there are an odd (even) number of neutrons (N) and an odd (even) number of protons (Z), an additional factor comes into play: nuclear pairing energy, which exhibits the same magnitude but opposite sign. This results in the division of the mass parabola into two distinct branches. Within the realm of nuclear ground states, a unique scenario can arise in which certain nuclei cannot decay into their nearest neighbor but instead have the capacity to decay into their second nearest neighbor nuclei. This process is known as double beta decay ($2\nu\beta\beta$) and it represents a higher-order process [16].

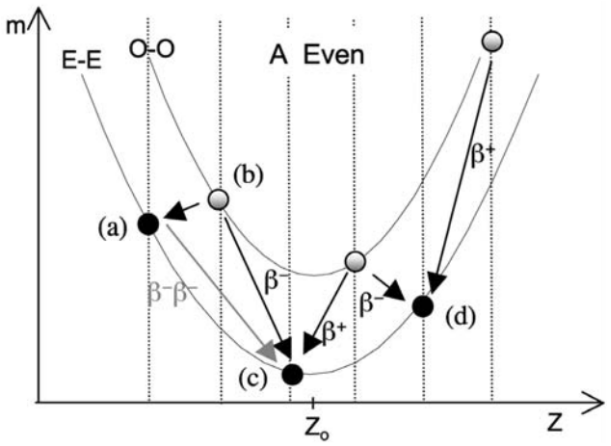

Figure 1.1 – The ground state mass parabola of A-even isobaric nuclei. Only the one within the even-even (E-E) shell (a), where β decay is inhibited (b), but could occur through two steps (c), are permitted to undergo double beta decay. The deviation in the parabola of odd-odd (O-O) nuclei is attributed to nuclear pairing energy. The figure and caption is from [16].

The corresponding decay is

$$(A, Z) \longrightarrow (A, Z + 2) + 2e^- + 2\,\bar{\nu}_e\ .$$

This decay is allowed by the Standard Model where two neutrons decay into two protons, two electrons (e^-) and two antineutrinos ($\bar{\nu}_e$) [17,18]. This decay process exhibits experimentally observed lifetimes of 10^{18} to 10^{21} years depending on the isotope [19]. In this decay, lepton number is conserved.

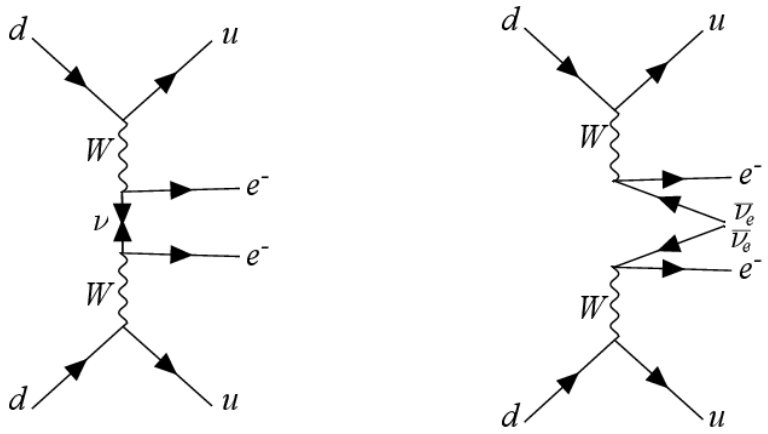

Figure 1.2 – Feynman diagrams at the quark level for the $0\nu\beta\beta$ decay (left) and for the $2\nu\beta\beta$ decay (right). Figure is from [20].

1.1.3.2 Neutrinoless Double Beta Decay

Another process is hypothesized to exist where neutrinos annihilate each other without appearing in the final state [11, 21]. In such decays no neutrino exists in the final state and it is called neutrinoless double beta decay ($0\nu\beta\beta$). Feynman diagrams at the quark level for the $0\nu\beta\beta$ decay and for the $2\nu\beta\beta$ decay are shown in Figure 1.2. $0\nu\beta\beta$ is the conversion of two neutrons in an atom's nucleus into two protons and two electrons [17, 18]. The pair of electrons are emitted quasi-simultaneously [19]. The corresponding decay equation is

$$(A, Z) \longrightarrow (A, Z + 2) + 2e^{-} \ .$$

The significant feature of $0\nu\beta\beta$ is its violation of lepton number conservation. Considering the fact that heavy nuclei do not carry significant kinetic energy and two electrons are the only remaining particles in the final state of $0\nu\beta\beta$, the summed kinetic energy of both electrons (K_e) approximates the mass difference of nuclei before and after the process. However, in $2\nu\beta\beta$ the mass difference of nuclei before and after the process are transferred to the kinetic energy of four particles (two electrons and two antineutrinos). Based on this fact, the distribution of electron energies for $2\nu\beta\beta$ and $0\nu\beta\beta$ has a significant difference as shown in Figure 1.3 [22].

$0\nu\beta\beta$ can only occur if the two following conditions are met:

— Neutrino particles have a Majorana nature [18].

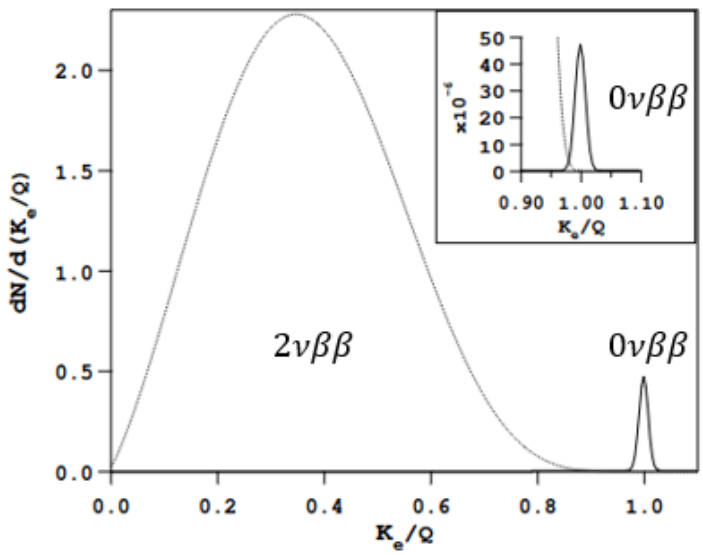

Figure 1.3 – Electron energy spectrum for $0\nu\beta\beta$ and $2\nu\beta\beta$. The assumed ratio of rates for $\frac{2\nu}{0\nu}$ is 10^2, and 10^6 in the inlay. Figure is from [23].

— There exists a neutrino with a non-zero mass (for at least one of the neutrino species) which can change its handedness between emission and absorption, or the weak leptonic current has a right-handed component [24].

If the decay rate of $0\nu\beta\beta$ aligns with predictions derived from experimental observations regarding neutrino masses, mixing, and specific occurrence conditions, it is suggested that Majorana neutrinos predominantly act as the mediators, as opposed to alternative sources of novel physics [25]. In this case, The probability per unit of time that a specific reaction will take place, known as the decay rate ($\Gamma^{0\nu}_{\beta\beta}$), can be calculated as the product of the phase space factor ($G^{0\nu}$), the squared matrix element ($|M^{0\nu}|^2$), and the square of the effective Majorana mass ($\langle m_{\beta\beta}\rangle^2$) [26]:

$$\Gamma^{0\nu}_{\beta\beta} = \frac{1}{T^{0\nu}_{\beta\beta}} = G^{0\nu} \cdot |M^{0\nu}|^2 \cdot \langle m_{\beta\beta}\rangle^2. \tag{1.1}$$

The phase-space factor is the function of the total energy of the system and the mass of the individual particles in the final state. In other words, it depends on the total released kinetic energy (Q-value) and the atomic number (Z) [21]. Results for $G^{0\nu}$ have been calculated with high precision for various nuclei [25].

If an experiment detects $0\nu\beta\beta$, the nuclear matrix element plays a pivotal role in deducing the effective neutrino mass [27]. The quantity $|M^{0\nu}|$ cannot be independently measured; its computation relies on a nuclear many-body theory, which is approached through various methodologies. The magnitudes vary, spanning from approximately 0.9 to 14, contingent upon the specific nucleus undergoing decay and the chosen theoretical framework [25].

The effective Majorana mass characterizes the strength of $0\nu\beta\beta$ decay. It is defined as the weighted sum of the neutrino mass eigenstates, considering their flavour composition and phase factors. The precise value of $\langle m_{\beta\beta}\rangle$ is still unknown, but it is constrained by various experimental and observational data, such as neutrino oscillation experiments, cosmological observations, and $0\nu\beta\beta$ searches. The current upper limit on $\langle m_{\beta\beta}\rangle$ is around 0.1 eV, which is much smaller than the masses of the charged leptons (electron, muon, and tau). Modern $0\nu\beta\beta$ experiments aim to demonstrate the Majorana nature of neutrinos and measure this effective Majorana mass [25].

1.1.3.3 Effective Majorana Mass

The effective Majorana mass can be described by:

$$\langle m_{\beta\beta}\rangle = \sum_i U_{ei}^2 m_i, \tag{1.2}$$

where m_i and U_{ei} are the neutrino mass eigenstate and the elements of the neutrino mixing matrix, respectively. The neutrino mixing matrix, also known as the Pontecorvo-Maki-Nakagawa-Sakata (PMNS) matrix, is a mathematical tool used to describe the phenomenon of neutrino oscillation [26]. The PMNS matrix relates the three flavour states of neutrinos (ν_e, ν_μ, and ν_{tau}) to the three mass states which are not identical to the flavour states. It is a 3×3 unitary matrix that depends on three mixing angles (θ_{12}, θ_{23}, θ_{13}) and one CP-violating phase (δ), which are all parameters that need to be determined from experimental data.

The PMNS matrix is given by [28] [29]:

$$|\nu_e\rangle = U_{e1}|\nu_1\rangle + U_{e2}|\nu_2\rangle + U_{e3}|\nu_3\rangle, \tag{1.3}$$

$$|\nu_\mu\rangle = U_{\mu 1}|\nu_1\rangle + U_{\mu 2}|\nu_2\rangle + U_{\mu 3}|\nu_3\rangle, \tag{1.4}$$

$$|\nu_\tau\rangle = U_{\tau 1}|\nu_1\rangle + U_{\tau 2}|\nu_2\rangle + U_{\tau 3}|\nu_3\rangle, \tag{1.5}$$

where $|\nu_e\rangle$, $|\nu_\mu\rangle$, and $|\nu_\tau\rangle$ are the flavour eigenstates of the electron, muon and tau neutrinos, respectively, and $|\nu_1\rangle$, $|\nu_2\rangle$, and $|\nu_3\rangle$ are the mass eigenstates of the three neutrinos. The coefficients U_{ei}, $U_{\mu i}$, and $U_{\tau i}$ are the elements of the PMNS matrix, which describe the probabilities of finding a neutrino of flavour i in the mass state j. The PMNS matrix provides a way to connect the measured fluxes of different neutrino flavours with the underlying neutrino mass spectrum. Determining the matrix elements is an active area of research in particle physics, with ongoing experiments aiming to improve the precision of the measurements [26].

1.2 Searching for $0\nu\beta\beta$ Decay

1.2.1 Liquid Xenon Time Projection Chamber

Scientists are searching for $0\nu\beta\beta$ in nine different isotopes: ^{48}Ca, ^{76}Ge, ^{82}Se, ^{96}Zr, ^{100}Mo, ^{116}Cd, ^{130}Te, ^{136}Xe, and ^{150}Nd [21]. Researchers consider a number of factors when designing an experiment, such as the natural abundance and cost for enrichment. Additionally, the techniques should be well understood and controllable in order to maximize the chances of making a discovery [21].

Isotope ^{136}Xe is one of the candidates for $0\nu\beta\beta$ experiments. The double beta decay of ^{136}Xe was discovered by the EXO-200 experiment [30, 31]. It undergoes a double beta decay to ^{136}Ba as can be seen in Figure 1.4. The probability of $0\nu\beta\beta$ is proportional to the fifth power of the atomic mass of the nucleus [32]. Therefore, isotopes with larger nuclear masses have a higher probability of undergoing $0\nu\beta\beta$. ^{136}Xe has a nuclear mass of 136 atomic mass units (amu), which is one of the largest among the naturally occurring isotopes.

Furthermore, ^{136}Xe has a half-life of about 2.17×10^{21} years [33]. Considering the fact that $0\nu\beta\beta$ decay is so rare, it requires a very large sample of atoms, a long observation time to detect and low background levels. ^{136}Xe has a high natural isotopic abundance of 8.87% [34]. However, with the use of centrifuge techniques, it is possible to enrich it to 80% or more in substantial amounts [35]. Xenon is a scintillating material with a high scintillation

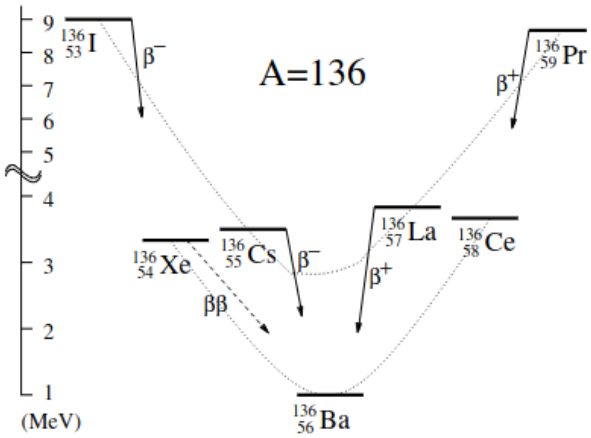

Figure 1.4 – Atomic masses of the isotopes with A = 136. Nuclei such as ^{136}Xe, ^{136}Ba, and ^{136}Ce are resistant to standard β decay, thereby manifesting their presence in the natural environment. Nevertheless, conservation of energy permits the double beta decay of ^{136}Xe to ^{136}Ba. Similarly, the decay of ^{136}Ce involves positron emission in a corresponding manner. The figure and caption are sourced from [23].

yield [36], meaning that it produces a relatively large amount of light for each unit of energy deposited within it. In addition, xenon has a fast scintillation decay time [37].

The Liquid Xenon Time Projection Chamber (LXe TPC) has extensive application in the investigation of rare events. A TPC, in general, is a type of particle detector for studying the trajectories of charged particles by using electric fields. When charged particles interact within the liquid medium, they generate both ultraviolet (UV) scintillation light and ionization electrons. The UV light has a relatively narrow spectrum, with a peak occurring at approximately 172 nm for xenon with a 14 nm FWHM [38, 39]. By measuring the ionization electrons on a segmented anode, after their drift through the detector, and by measuring the time difference between their arrival on the anode and the prompt scintillation light, the location, multiplicity and energy deposited of each event can be reconstructed. A schematic illustrating the operation of an LXe TPC is presented in Figure 1.5.

Detectors also employ electroluminescence to enhance the ionization signal. Then electrons are accelerated in xenon gas (typically around 3-5 kV/cm/bar), secondary electroluminescent vacuum-u;tra-violet (VUV) light is emitted. By adjusting the electric field, it's possible to produce a substantial number of photons (approximately 1000) per electron that

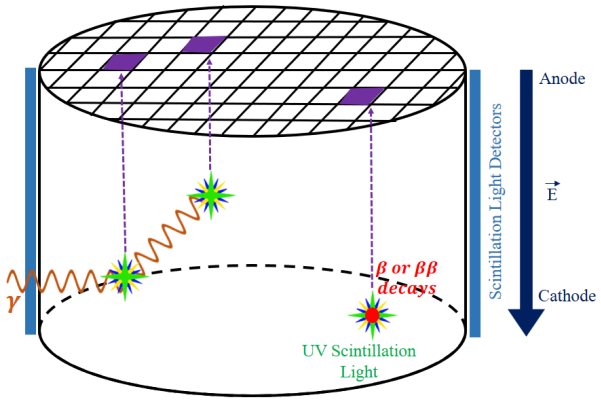

Figure 1.5 – A diagram illustrates a single-phase TPC that measures both charge and scintillation light, utilizing the anticorrelation between these two data points to enhance energy resolution.

reaches the anode, resulting in a signal that is proportional to the initial ionization. This EL technique permits the simultaneous measurement of both the scintillation (S) and ionization (I) signals using the same photosensors [38, 40].

One noteworthy characteristic of LXe is the presence of anti-correlated fluctuations in the charge and light signals [41]. When energy is deposited in LXe, the released charges can take two paths: they may either recombine with xenon atoms, leading to the emission of scintillation light, or they can be guided towards an anode under the influence of the electric field. This property allows for the fine-tuning of energy resolution based on the expected efficiencies of charge and light collection.

LXe has a density of approximately 3.1 g/cm^3 at the triple point at 161 K and a high atomic number. These characteristics result in large gamma ray interaction cross-sections and short attenuation lengths. As a result, LXe acts as a natural shield against external background radiation. The monolithic nature of a tonne-scale LXe TPC allows to capture and retain the full energy deposited by a single gamma ray even after multiple Compton scatters. The high density of LXe enables the construction of compact detectors compared to gas-phase technologies. This compact design allows for a higher concentration of $0\nu\beta\beta$ candidate nuclei within a smaller volume [42].

1.2.2 The EXO-200 Experiment

The EXO-200 (Enriched Xenon Observatory) experiment was designed to detect $0\nu\beta\beta$ in ^{136}Xe. The experiment was located at the Waste Isolation Pilot Plant (WIPP) in New Mexico, USA with 1,585 metres-water-equivalent shielding. WIPP is a salt mine which has the advantage that salt is less radioactive than hard rock [43]. EXO-200 consisted of a cylindrical vessel filled with a total of approximately 175 kg of liquid xenon enriched to 80.6% in ^{136}Xe, out of which 110 kg was present in the active detector volume, and the rest was situated in the gas handling system [44]. This vessel was surrounded by arrays of avalanche photodiodes (APDs) and wire planes to detect the emitted scintillation photons and ionization electrons in the liquid xenon respectively. Several layers of shielding were added to minimize background radiation, including that stemming from detector components, potential gamma ray leakage through passive shields, and external radon (^{222}Rn) interference.

The EXO-200 TPC was composed of two identical cylinders with a shared semi-transparent cathode and two pairs of anode wire planes. The mesh cathode was held at a high voltage, creating an electric field that directed electrons produced by interactions in the liquid xenon toward the anode [44].

To reduce background, the experiment used a combination of shielding materials, including lead, copper, and HFE-7000 cryofluid, along with a muon veto system to identify events caused by cosmic rays [44]. EXO-200 also used a technique called pulse shape discrimination, which can distinguish between signals produced by electrons and those created by gamma rays [45].

Muons that pass through the TPC are easily identified as background because they leave behind a large amount of energy and create signals that look like tracks [44]. An external muon veto system is needed to tag muon bremsstrahlung, gamma rays emitted by nuclear excitation induced in the detector components, and spallation neutrons. The muon veto system identifies and excludes events involving muons from the analysis because they can mimic the signals from other particles or introduce unwanted backgrounds. These detectors are composed of scintillator panels that are sensitive to muons and can detect the particles passing through them. If a muon is detected, the data from that event is discarded or flagged

for further investigation to ensure that only events without muons are used in the analysis. The muon veto system is placed around the experimental apparatus.

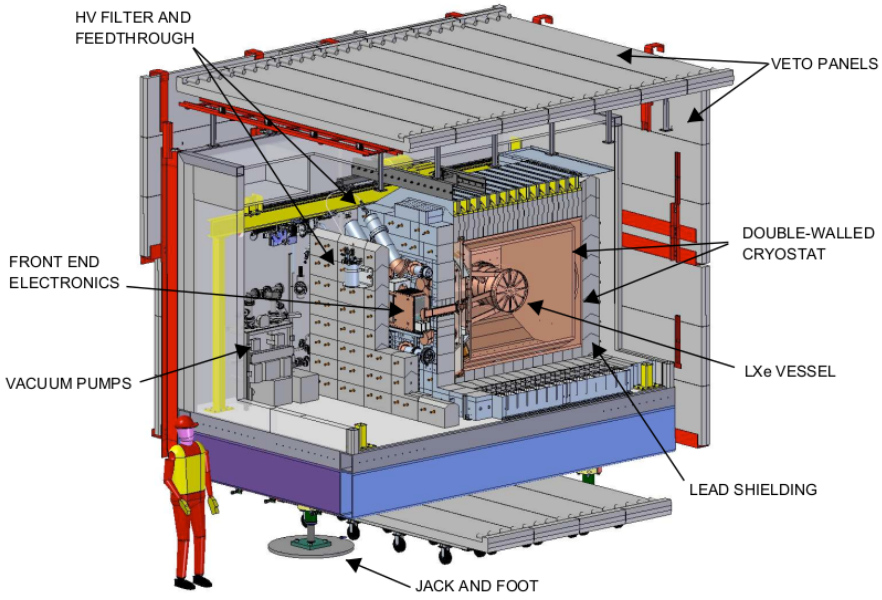

Figure 1.6 – Sectioned view of the EXO-200 setup. A thin-walled quasi-cylindrical copper vessel houses the TPC and the LXe. The outermost shielding layer, a 25 cm thick lead barrier, envelops the outer vessel of the cryostat. Surrounding the cleanroom that houses the remainder of the detector is a cosmic-ray veto counter constructed from plastic scintillators. Sourced from [44].

The muon veto system of the EXO-200 experiment, in fact, consisted of an array of plastic scintillator panels installed externally on four of the six sides of the clean room module containing the TPC (Figure 1.6). Each panel had four 2-inch photomultiplier tubes (PMTs) attached to the ends of light guides with optical cement to detect the scintillation light. To increase light collection, the panels were wrapped in crinkled aluminum foil. The underside of each panel was covered by 4 cm of borated polyethylene, which not only provided structural support but also acted as a partial thermal neutron shield for the TPC. The veto detector was comprised of 232 PMTs that were grouped in sets of four and matched for gain. The PMTs on each end of the panel were powered by a single high-voltage channel and were read out together. Based on simulations and measurements, it was estimated that the efficiency of the veto detector in identifying muons passing through the TPC was over

95%. The main reason for inefficiency was the incomplete coverage of the clean room by the scintillator panels [44].

EXO-200 took data from 2011 to the end of 2018 and has set stringent limits of 3.5×10^{25} years at the 90% confidence level on the half-life of $0\nu\beta\beta$ in ^{136}Xe [46]. It also reported the observation of $2\nu\beta\beta$ in ^{136}Xe with a half-life of 2.17×10^{21} years [30].

1.2.3 The nEXO Experiment

The nEXO experiment will build on the success of EXO-200 by using a larger volume and aiming for a higher enrichment factor, along with advanced detector technologies and background rejection techniques. nEXO's larger size and its ability to maintain extremely low background levels, along with its use of the TPC technique for analysis, greatly improves its sensitivity compared to EXO-200. Figure 1.7 shows nEXO's projected sensitivity as a function of its livetime which reaches 1.35×10^{27} years at a 90% confidence level after 10 years of data taking. It is also projected to have a 3σ discovery potential of 0.74×10^{28} years for the same amount of data [47].

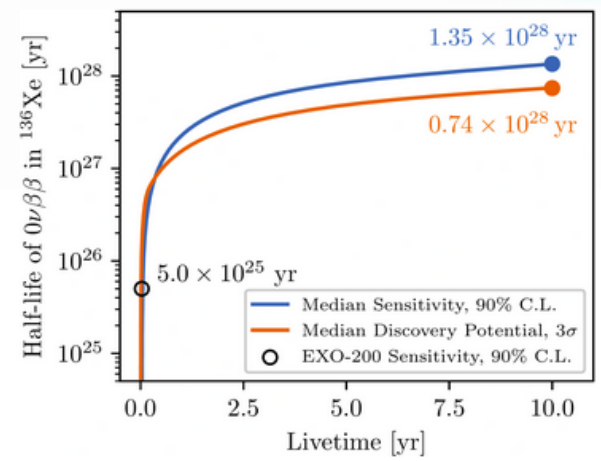

Figure 1.7 – Projected sensitivity and median discovery potential as a function of livetime of nEXO. The final sensitivity of EXO-200 of 5.0×10^{25} years is shown for comparison. This picture originates from [48].

The nEXO experiment aims to detect $0\nu\beta\beta$ by using a TPC filled with 5 tonnes of liquid xenon (LXe), encompassing approximately 2×10^{28} nuclei, enriched to 90% in ^{136}Xe [47, 49].

LXe TPCs offer several advantages, including a large, uniform mass of the required isotope, three-dimensional event vertex reconstruction, and good energy resolution. Another benefit of LXe TPCs is the ability to recirculate the active material, leading to improved purity over time. As the detector size increases, the benefits of using LXe TPCs become even more significant due to the improved scalability and inherent capabilities of LXe as a self shielding TPC [49]. When the detector volume increases, the surface-related backgrounds decrease because the particles or events originating from the surfaces are farther away from the fiducial volume.

The nEXO detector measures both scintillation light and drifting ionization signals and combines them to create three-dimensional reconstruction of the event vertex (energy, location, and event multiplicity). The detector will use event reconstruction topology to distinguish between double beta decay events and background events, which are usually caused by gamma radiation. Beta-like events in a LXe medium generally have energy concentrated in one location. In contrast, background events from gamma sources result in energy deposited in multiple locations with decreasing event rates toward the center of the detector due to attenuation within the dense LXe. Alpha events can be rejected by their diffident scintillation to ionization yield which is caused by the higher ionization density in LXe by these particles [49]. The energy measurement will use independent measurements of scintillation and ionization signals and take advantage of the anticorrelation between the two to achieve a resolution that can reject $2\nu\beta\beta$ background events to negligible levels at the Q-value [44, 49]. Figure 1.8 shows the anticorrelation between light and charge signals and the improvement in energy resolution in EXO-200.

The nEXO TPC has a cylindrical shape made of electroformed copper with a diameter and inner height of 127.7 cm [47]. When taking into account the volume displaced by internal components and using a density of 3.057 gcm^{-3} [47] for enriched xenon, the total mass of contained LXe is 4811 kg. All materials composing the TPC require the most rigorous screening to ensure sufficiently low radioactive backgrounds [47].

The LXe TPC is surrounded by a multilayered shielding system. Illustrated in Figure 1.9 is the nEXO detector design, featuring a TPC filled with enriched LXe. The TPC is enclosed by around 33,000 kg of HFE-7000, a refrigerant fluid with a substantial heat capacity utilized

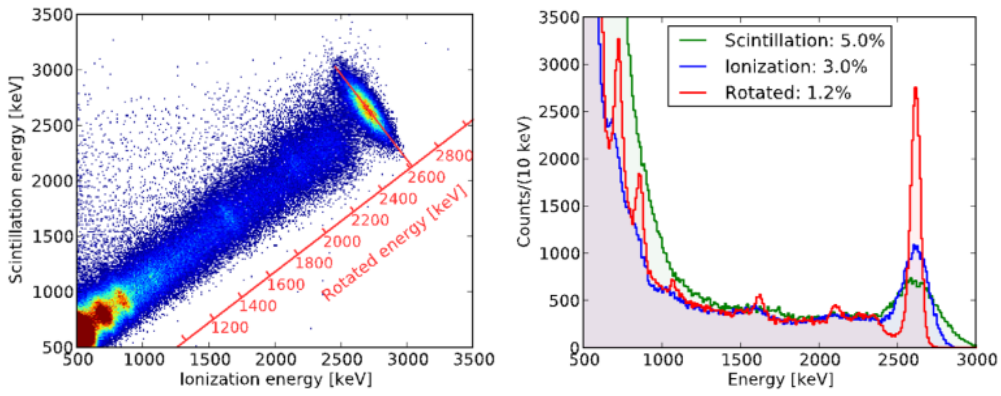

(a) **(b)**

Figure 1.8 – Calibration data for the "Single Site" events (refers to the number of spatially separated energy depositions inside the chamber) in EXO-200, derived from a ^{228}Th source. An anticorrelation between light and charge signals can be seen in the picture (a). The energy resolution is improved when the optimal linear combination of scintillation and ionization is used for the energy measurement (b). The picture and caption sourced from [49].

to maintain the xenon in a liquid state. This configuration serves the dual purpose of acting as both a radiation shield and a thermal bath [47]. The HFE-7000 acts as an effective shield against gamma rays due to its density of around 1.8 gcm^{-3} at 170 K [47, 49]. The cryostat comprises an Inner Vessel (IV) and an Outer Vessel (OV), separated by a vacuum layer, providing thermal insulation from the Outer Detector (OD), an active water shield [47, 49].

1.2.3.1 The nEXO Outer Detector

Using large water tanks to shield against external backgrounds and detect muon passage is a popular method due to its cost-effectiveness, the ability to seal it tightly, and the option to instrument it with Cherenkov light counters. Although water has a low density, which requires a thicker shield, its high hydrogen content makes it well-suited for neutron moderation. Additionally, the light nuclei in water minimize the production of neutrons by cosmic-ray spallation [49].

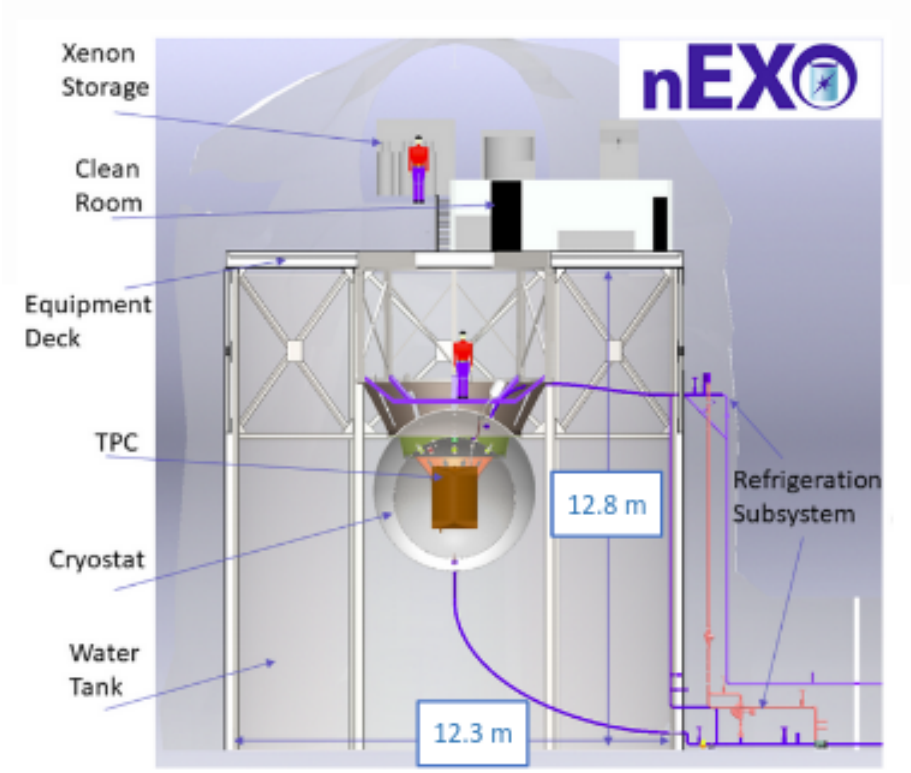

Figure 1.9 – Sketch of the nEXO detector concept. It illustrates the LXe TPC situated in a vacuum-insulated cryostat filled with HFE-7000 refrigerant fluid which acts as the innermost gamma-ray shield. The Outer Detector is composed of a large water tank, which provides shielding against neutrons and gamma radiation from the rock cavity and external detector components. The sketch assumes that the detector will be placed in the Cryopit at SNOLAB. The picture is obtained from [49].

The nEXO OD represents a substantial shield that completely envelops the TPC and cryostat. Comprising 1.5 tonnes of ultra-pure, deionized water, it serves as a crucial component of the setup. This system is employed to meet three goals [49]:

— It protects from external radiation, e.g. the gamma radiation from the surrounding rock.

— It moderates and stops neutrons generated by radioactive decays in the walls of the underground cavern.

— It functions as a Cherenkov detector; detecting cosmic radiation, specifically muons that pass through the water, which may result in correlated events in the TPC.

Passive shielding alone is sufficient for the first two items, while instrumentation is required to detect cosmic muons. In light of this, the OD is instrumented by an array of PMTs, enabling it to operate as a water-Cherenkov muon veto detector.

The design of the OD geometry presented here is intended for installation at SNOLAB's Cryopit. Based on modelling, a minimum diameter of 11 m and a height of 12 m is sufficient to shield against background contributions from the cavern rock and concrete and to achieve near-maximal muon tagging efficiency when PMTs are mounted on the tank walls to detect Cherenkov light in the water. The simulated nEXO geometry includes a water tank that is 12.3 m in diameter and 12.8 m in height, which is compatible with the current dimensions of the Cryopit [47]. The larger dimensions are chosen to be conservative with respect to shielding.

Approximately 500 PMTs with an 8-inch diameter (specifically the Hamamatsu 10-stage model R5912) are available for the nEXO muon veto. They are decommissioned from the Daya Bay experiment [50]. The preliminary baseline design assumes that 125 of the Daya Bay PMTs will be installed in nEXO's muon veto. To enhance the efficiency of photon collection, all inner surfaces of the water tank will be coated with a highly-reflective material. The reflectance is diffuse with a small specular component [49].

Simulations indicate that the current OD design achieves a muon tagging efficiency of $(99.6 \pm 0.4)\%$. To optimize the muon veto performance, we conducted studies where we varied the number and placement of PMTs inside the tank, along with different trigger conditions (coincidence time windows). By taking into account the anticipated 2% annual

Figure 1.10 – Photo of a waterproof PMT assembly from Daya Bay, including PMT, base, cable, magnetic shield and supporting bracket. Picture and caption are sourced from [49].

failure rate of PMTs, observed by Daya Bay, this analysis enables us to estimate the total number of PMTs needed for a 10-year operation. Our findings indicate that installing 125 8-inch PMTs across all tank surfaces will meet nEXO's muon veto requirements [42].

Each PMT has been pre-assembled with a μ-metal magnetic shield and bracket [51], subsequently mounted onto a Tee support structure, which is affixed to a wall module as shown in Figure 1.10. These PMTs were specifically engineered to withstand pressures of up to 7 atm, significantly exceeding the maximum pressure within the nEXO muon veto system at SNOLAB.

Intended for operation with a positive high voltage, these PMTs are furnished with a single 50 Ω coaxial cable tailored for use in ultra-pure water. To ensure their performance longevity, the stability of timing and gain will be closely monitored through a calibration system. Additionally, a periodic trigger within the DAQ system may be employed to facilitate continuous PMT gain calibration using dark noise [49].

Chapter 2

The Outer Detector Calibration Systems

In large-volume, low-background experiments such as the nEXO experiment, the creation of a calibration system holds considerable importance. Every component of the experiment requires a system to monitor its operational reliability. Particularly, the OD, which serves as a muon veto system, necessitates a calibration system to guarantee its faultless operation. Drawing inspiration from established calibration systems employed in analogous experiments offers a valuable approach for formulating a calibration strategy for nEXO.

2.1 Importance of Having a Calibration System

Research aimed at detecting rare decays, like the $0\nu\beta\beta$ decay, requires a careful and precise design. Each part of the experiment needs thorough scrutiny, considering the influence of different materials. The implementation of carefully designed calibration systems across different parts of these experiments is crucial for ensuring the accuracy, reliability, and consistency of the collected data. This is also true for the nEXO experiment—a detector of large-volume and low-background, purpose-built for the realm of rare event physics. In this context, calibration systems play an important role in facilitating the meticulous and regular assessment of the performance parameters of the system's components, all while mitigating the risk of radioactive contamination [52].

Within the nEXO experiment, the OD stands as a significant component. As outlined in the first chapter, the OD functions as a radiation shield, completely immersing the TPC and cryostat. This immersion serves the purposes of shielding the system from external radiation and moderating neutrons, all while acting as a Cherenkov detector. An array of PMTs enables the OD to operate as a muon veto detector. While the main constituents of the OD—water and PMTs—may seem straightforward at a glance, both elements demand rigorous monitoring. The efficacy of the PMT array's performance and its responses must be validated an monitored. Similarly, the water quality must meet stringent criteria. Consequently, the development of a calibration system tailored to the OD is important to fulfill these objectives.

The design of the OD calibration system should be multifaceted, capable of capturing diverse parameters. This encompasses the response of PMTs with respect to light intensity, the timing characteristics of PMTs' readout systems, light scattering and absorption within the water, and the optical properties and quality of the water. A paramount consideration in designing the calibration system is minimizing the presence of potentially radioactive materials in close proximity to the inner detector [52]. Addressing this concern, the monitoring system for the OD calibration is situated outside the active detector volume.

To design an effective calibration system, one approach involves a thorough examination of successful systems utilized in similar experiments. This entails assessing their merits and drawbacks when adapted to nEXO's requirements. In the case of developing a calibration system for nEXO's OD, our analysis considered the calibration systems of four experiments: SNO+, XENON1T, LUX-ZEPLIN (LZ), and GERDA. Drawing from these insights, we tailored a custom calibration design specifically suited for nEXO's OD. This chapter offers a concise overview of these various calibration systems.

2.2 Overview of Calibration Systems

2.2.1 The SNO and SNO+ Experiments

The SNO (Sudbury Neutrino Observatory) experiment was a neutrino detection experiment that used heavy water as a target to detect neutrinos from the Sun and provided crucial measurements for the solution to the solar neutrino problem [53].

Calibrating the PMTs in SNO was done using a laserball. A laserball is simply a light diffusing optical object capable of emitting light isotropically and at different wavelengths. It is a sphere made up of a quartz flask. The flask contains tiny silica beads suspended in clear silicone gel. A quartz optical fibre is connected to the center of the flask and is part of the umbilical that connects the laserball located in the detector volume to the laser on the deck [54]. The light inside the source has a scattering length of approximately 1 centimeter, which is a good balance between having good isotropy (necessitating short scattering length) and minimizing intensity losses due to dispersion and absorption (necessitating a large scattering length) [55]. A picture of the laserball is shown in Figure 2.1.

Figure 2.1 – A photo of a laserball illuminated by a laser diode, employing an acrylic light guide for light propagation. The picture is from [56].

The SNO+ experiment is an upgraded version of the SNO experiment. Several changes were made to SNO+ compared to SNO, including new scintillator material, trigger, processing and purification systems, front-end readout electronics, and calibration systems. SNO+

uses liquid scintillators, Linear Alkylbenzene (LAB) with PPO (2,5-diphenyloxazole), instead of heavy water. Its primary aim is to search for $0\nu\beta\beta$ after Te-130 loading and measure different types of neutrinos. Its main objective is to study neutrinos from various sources, such as the Sun, the Earth, supernovae and nuclear reactors [57].

The SNO+ detector is situated 2092 meters underground at SNOLAB, protected against cosmic rays. The innermost detector volume is shielded by ultra-pure water to shield against natural radioactivity in the rock. The detector is made up of a large spherical acrylic vessel (AV), 12-meter diameter, with a 5 centimeters thick wall, surrounded by around 9500 PMTs placed in a steel support structure. Each PMT has a reflector to increase its optical coverage [57].

Liquid scintillator generates more light per event, allowing for a lower threshold energy down to the megaelectron volt range for measurements of solar neutrino elastic scattering signals. However, this increases sensitivity to backgrounds and requires an exact calibration system. To meet the radio purity requirements, the deployment of calibration sources must be minimized or eliminated if possible. Therefore, a system for monitoring and calibrating the PMT array has been designed to be installed permanently outside the detector's active volume [52].

Known as the External LED/Laser Light Injection Entity (ELLIE), the complementary system had been developed to monitor the PMT timing and gain, as well as the scintillator properties. ELLIE is comprised of three subsystems, namely Attenuation Monitoring (AMELLIE), Scattering Measurement (SMELLIE), and Timing (TELLIE). Each of the three subsystems in ELLIE utilizes infrastructure on the deck to generate optical pulses, which are then transmitted into the AV through optical fibres [56]. A schematic of this calibration system is presented in Figure 2.2.

To monitor the stability of scintillator attenuation in-situ, AMELLIE utilizes LEDs at various wavelengths and injects light at four different locations in two directions. Wide-angle quartz fibres are employed to ensure adequate coverage. SMELLIE employs four lasers with wavelengths of 375, 405, 440, and 500 nm. These lasers are connected through an optical fibre switch to twelve quartz fibres that terminate at four different locations. At these locations, each fibre is connected to a collimator that points in three different directions, 0, 10, and

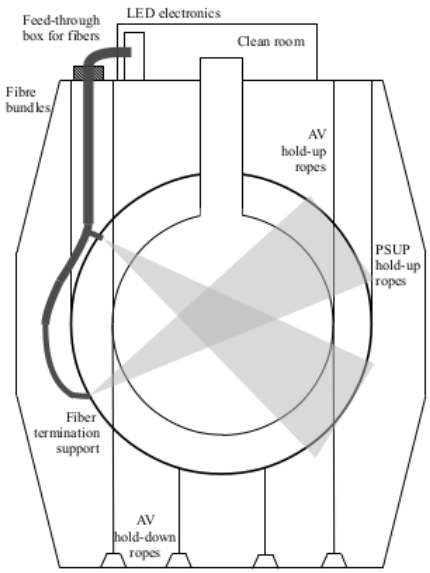

Figure 2.2 – Illustration of the SNO+ detector's layout, depicting the calibration apparatus positioned on the upper platform adjacent to the AV. Additionally, a representation of the illumination sources for light injection is provided. The picture is from [52].

20 degrees, relative to the center of the detector. By analyzing the position and timing of PMT hits with respect to the initial beam direction, SMELLIE measures the scattering of the scintillator. Multiple injection points and directions are used to check for systematic errors. TELLIE uses LEDs that emit light at a single wavelength, and the light is injected into each of the 91 PMT support structure nodes and one at the neck of the AV through fibres [56].

Based on the information provided, the design consists of two main components; LEDs and fibres. To achieve the desired performance, an LED with a low resistance of 9 Ω was chosen. The differential resistance is gauged in the nearly linear section of forward current versus forward voltage, specifically above the LED threshold voltage. Since only a few specific LEDs were needed in this design, the LEDs were coupled to the optical fibres by drilling the LED lens to create a socket. The LED and fibre are enclosed within a coupler that also holds a photodiode positioned opposite the LED to monitor the average light level entering the fibre. The digitalized output from this photodiode will be incorporated into the data stream, offering an assessment of the light intensity reaching each PMT. This assessment remains

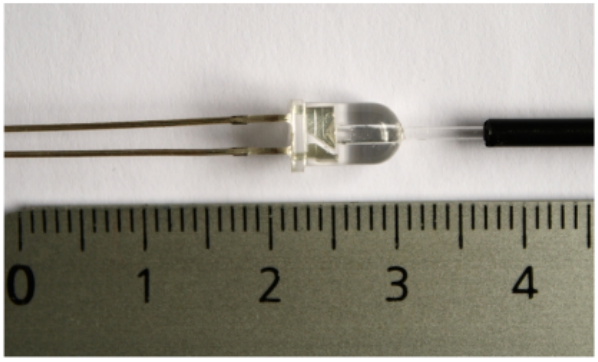

Figure 2.3 – LED module with an affixed optical fiber, achieved through perforation. The picture is from [52].

independent of the LED driver settings [52]. Figure 2.3 illustrates an LED connected to the optical fiber.

Aside from calibrating the PMTs in SNO+ using the ELLIE system, the experiment also requires in-situ calibration of the detector medium's optical properties. Although the laserball is utilized for this task, it is necessary to continuously monitor the optical properties between source deployments. To address this, an extension of the LED-based system is being developed to monitor optical attenuation. This system consists of eight additional optical fibers with a narrower angular profile, which are paired with LEDs of different wavelengths. The completed attenuation monitoring system operates using the same driver and control circuitry as the PMT calibration system [52].

The design of the calibration system for the SNO+ PMT array is to use an LED-based system to inject light into a detector, with the light source placed on the deck above the detector. This is done to minimize the presence of potentially radioactive materials near the detector core and allow for easy access during maintenance. The main purpose of the PMT calibration system is to measure and track three values: PMT time offset, discriminator time walk, and gain [52].

2.2.2 The XENON1T Experiment

XENON1T is an experimental facility designed to detect dark matter particles. It is located at the Gran Sasso National Laboratory (LNGS) in Italy, which is an underground

research facility [58]. XENON1T has been one of the most sensitive dark matter experiments to date. It started collecting data in 2016 and operated until late 2018. During its operation, it set stringent constraints on the properties of dark matter particles, significantly narrowing down the possible parameter space for dark matter models.

The muon veto system of XENON1T consists of a water tank with a diameter of 9.6 m and a height of 10.2 m. The water tank is equipped with 84 PMTs to make up the Cherenkov muon veto system. These PMTs (Hammamatsu R5912ASSY) have a quantum efficiency of approximately 30% for wavelengths between 300 nm and 600 nm and a mean gain of 6×10^6 for a bias voltage of 1500 V. The PMTs are set with a threshold that allows for the detection of single photoelectrons with an efficiency of around 50% [58].

The detector setup includes three arrays of PMTs positioned at different heights and orientations within the water tank to optimize detection efficiency. These arrays are referred to as the Top Array, Lateral Array, and Bottom Array. The Top Array is located at a vertical height of 9 m from the ground floor, specifically at the top edge of the cylindrical part of the tank. The PMTs in the Top Array are positioned to look downward, facing toward the interior of the tank. The Lateral Array consists of rings that are evenly spaced vertically and attached to the surface of the tank. The PMTs in this array are oriented to look inward, towards the center of the tank. The Bottom Array is positioned on the bottom surface of the tank, specifically at a radius of 4.5 m. The PMTs of the Bottom Array are directed upward, facing toward the top of the tank [59]. The top and bottom rings consist of 24 evenly spaced PMTs, while the Lateral Array consist of three rings at heights of 2.5 m, 5.0 m, and 7.5 m each have 12 PMTs [60].

Two independent calibration systems are employed to ensure the calibration and equalization of the PMTs in the muon veto system [60]:

— Optical Fiber Calibration: Each PMT can be calibrated individually using an optical plastic fibre positioned in front of it. The fibre carries light emitted by a blue LED with a wavelength of 470 nm. The LED is driven by voltage and connected to a bundle of eight optical fibres grouped together at one end. The other end of the bundle is attached to a vertical support located next to the PMT. A surface made of PTFE

(polytetrafluoroethylene) is affixed to the vertical support to reflect the light toward the PMT.

— Diffuser Ball Calibration: The second calibration system uses four diffuser balls positioned inside the water tank. These diffuser balls emit light that illuminates all the PMTs in the system.

Figure 2.4 provides a schematic representation of these two calibration systems, along with a depiction of the positioning of the PMTs within the muon veto system.

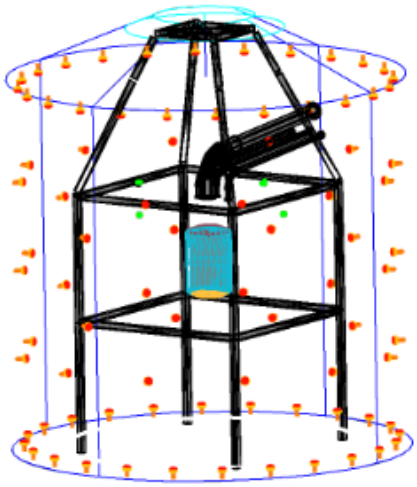

Figure 2.4 – Blue LED light is used to calibrate PMTs through a fibre. Furthermore, light emitted from four diffuser balls is employed to measure the entire system's response. Green dots demonstrate the position of four diffuser balls. The illustration was taken from [58, 60].

2.2.3 The LUX-ZEPLIN (LZ) Experiment

The collaborative LUX-ZEPLIN (LZ) experiment, situated at the Sanford Underground Research Facility (SURF) in Lead, South Dakota, USA, is a second-generation dark-matter detector with the goal of directly detecting dark matter particles interacting with ordinary matter. With its liquid xenon mass of around 10 tonnes, LZ is projected to outperform all other experiments in terms of sensitivity for identifying weakly interacting massive particles within this mass range before the end of the decade [61].

The OD of the LZ experiment consists of vessels, forming a hermetic structure. Utilizing segmented vessels allows for cost-effective fabrication at the manufacturer's facility. The chosen sizes of the vessels enable easy insertion and assembly within the water tank. The OD is composed of ten acrylic tanks that contain around 17 tonnes of gadolinium-loaded liquid scintillator. Monitoring this setup is a set of 120 inward-facing 8-inch Hamamatsu R5912 PMTs, mounted on stainless steel frames within the water tank. Low-density water displacers will fill the gaps between the cryostat and the acrylic vessels and around the penetrations to minimize the chances of light absorption in an inert material. Additionally, a white diffuse reflector will be placed inside the OD vessels to enhance scintillation light collection [61, 62].

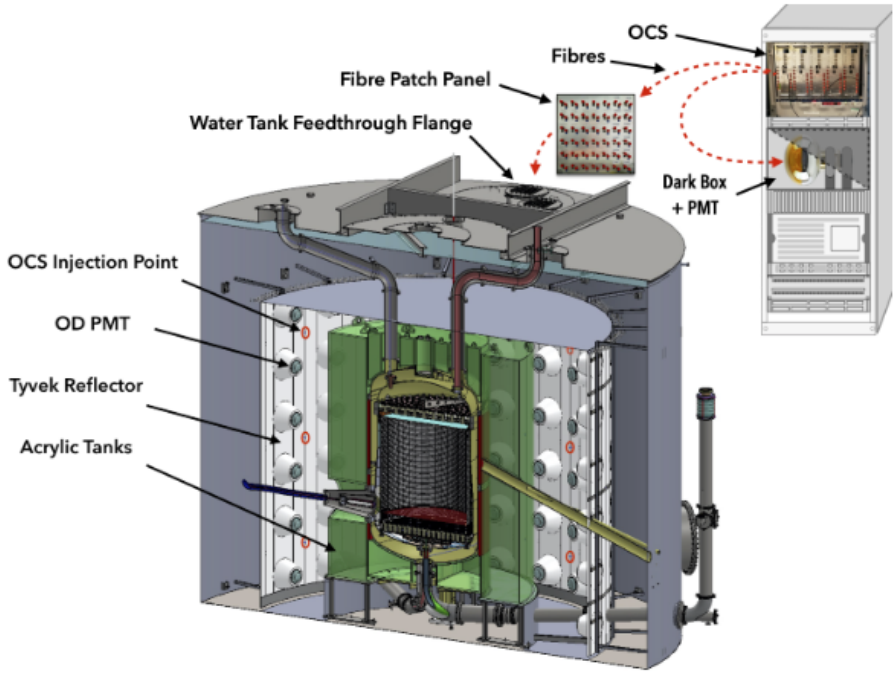

Figure 2.5 – An overview of the LZ detector systems. Positioned at the center is the LXe TPC. Surrounding the TPC are the scintillator tanks, represented in green, along with the light collection system, depicted in white. All of these components are contained within a large water tank, shown in a blue-grey shade. Several injection points for the OD optical calibration system are indicated by red circles. The illustration was taken from [62, 63].

The experiment can achieve its intended sensitivity to detect dark matter by maintaining the required performance of the veto system. To achieve the required efficiency of the veto

system and ensure that LZ meets its sensitivity goals, an optical calibration system has been developed and implemented [62]. This system serves several purposes; it allows for cross-calibration of the water PMTs, ensuring consistent and accurate measurements of signals throughout the experiment's duration. Additionally, it enables the monitoring of optical properties in both the water and the scintillator [61]. Figure 2.5 displays the design of the LZ detector system, including several injection points for the optical calibration system.

The optical calibration system will employ duplex optical fibres to deliver controlled light pulses generated by LEDs to 35 specific locations within the OD. Of these locations, 30 are evenly distributed around the water tank, covering ten positions in azimuth at three different heights. This arrangement ensures comprehensive coverage of the detector. There are four injection points beneath the four side scintillator tanks to assess the quality of the scintillator and one injection point below one of the side scintillator tanks to assess the quality of the acrylic material [62].

2.2.4 The GERDA Experiment

The GERDA (Germanium Detector Array) experiment is a scientific collaboration investigating the nature of $0\nu\beta\beta$ decay. The experiment is conducted deep underground at the Laboratori Nazionali del Gran Sasso (LNGS) in Italy. GERDA aims to achieve a high sensitivity to detect extremely rare decay events by minimizing background interference [64]. GERDA has undergone several phases, with each phase involving an increase in the number of germanium detectors and improvements in the background suppression techniques. The latest phase of the experiment significantly increased the number of detectors to enhance the experimental sensitivity.

The muon veto system for the GERDA experiment consists of three separate detector systems, as illustrated in Figure 2.6. The first system involves 36 plastic scintillator panels positioned on the roof of the GERDA cleanroom, precisely above the neck of the cryostat. Its purpose is to detect muons that directly traverse through the cryostat's neck. The second system employs the water tank, which serves as an active muon Cherenkov veto. The water tank is equipped with a total of 60 PMTs. These PMTs are arranged in a specific configuration of four rings, each comprising 10 PMTs and are positioned along the height of

the water tank. Additionally, 20 more PMTs are placed in two rings encircling the bottom of the water tank, surrounding the cryostat. The muon veto is augmented by an additional compact water Cherenkov detector situated below the cryostat. This detector incorporates 6 PMTs and is designed to detect muons that travel directly from above, pass through the cryostat, and ultimately reach the veto system [65].

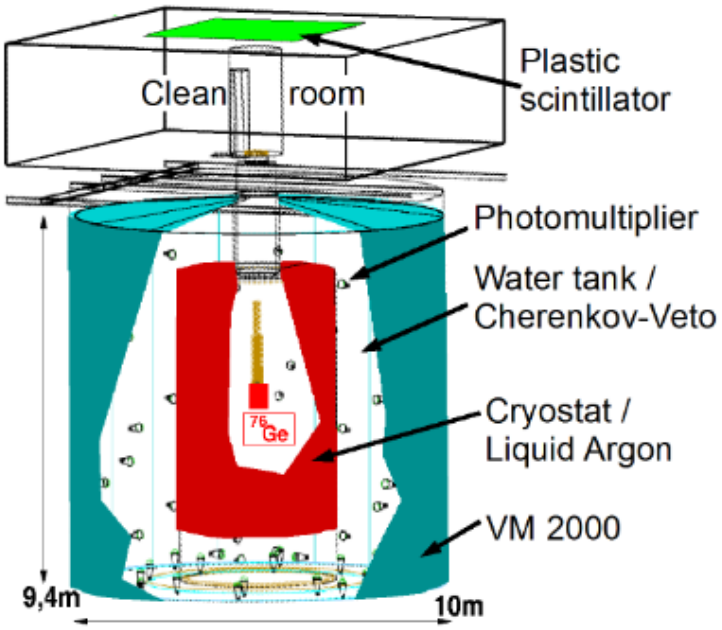

Figure 2.6 – The figure illustrates the muon veto system utilized in the GERDA experiment. In the center, the cryostat is displayed, containing the germanium detectors. Surrounding the cryostat is the water tank. Above the cleanroom area, the plastic scintillators are positioned as part of the muon veto system. The illustration was taken from [65].

Continuous monitoring and calibration are essential to ensure the proper functioning of the PMTs throughout the experiment's duration. Consequently, two systems of light pulses have been developed for this purpose.

The first system incorporates a single fast ultra-bright blue LED. The light emitted by a single LED will be transmitted to all PMTs through optical fibres, enabling a comparison of the signals produced by different PMTs illuminated by the same light source. The intensity of the light emitted by the LED can be adjusted within a range of 0 to 10^9 photons per pulse, with pulse durations ranging from 3 to 10 ns [65, 66].

The second system will utilize five diffuser balls, each featuring a single high-power blue LED positioned within the water tank. Four of these diffuser balls will be placed within the water tank, while one ball will be located in the volume below the cryostat. They emit a fixed amount of 10^{12} photons per pulse and have a pulse width of 10 ns. The use of these diffuser balls not only provides geometrically dependent responses from the PMTs but also offers timing information due to the varying distances between the PMTs and the diffuser balls [64–66].

Optical fibres are used to transmit the light to each diffuser ball. The diffuser balls are glass bulbs with an approximate diameter of 50 mm. The inner volume of the bulbs is filled with a mixture of silicone SilGel 612 A&B blended with S32 glass bubbles. A small glass bulb is placed in the center of the volume, and the optical fibre is directed to this innermost part. In this central volume, a mixture of Lensbond and S32 glass bubbles is used as the filling material [65, 66].

2.2.5 The nEXO Experiment

After reviewing the calibration systems employed in similar experiments, we have formulated an approach for calibrating the muon veto system of the nEXO experiment. Our aim has been to create a simple calibration system while ensuring longevity in its functionality. This system must fulfill calibration requirements, including the calibration of timing properties of the PMT's readout system and the continuous monitoring of the water's optical properties.

Following the approach employed in successful muon veto calibration systems like those used in XENON1T, LZ, and GERDA, the calibration system for the nEXO OD will adopt a unified strategy. This involves using a laser/LED fiber optic system placed within the water tank. Chapter three of this thesis will explore the detailed design and selection process for each component in our calibration system. Additionally, chapter four will present the results from our simulations, which will play a crucial role in refining and precisely defining the calibration system.

Chapter 3

Defining the nEXO Outer Detector Calibration System

Based on the purpose of the calibration system and taking factors into consideration, the calibration system of the OD of the nEXO experiment will consist of three main components: laser sources, optical fibers, and diffuser balls. This chapter will focus on a detailed examination of the properties inherent to these individual components. The ensuing chapter will subsequently showcase the outcomes achieved through the implementation of this system, drawing Chroma [67] simulation results.

3.1 Outer Detector Geometry

The geometry of the OD and the precise positioning of each PMT matter in developing an efficient calibration system for the nEXO OD. In the current geometry which is used in the simulation, there are five components, as depicted in Figure 3.1, each serving a specific function within the experimental framework. The setup comprises a water tank containing ultra-pure water as its medium. Suspended at the center of this volume is a cryostat with an outer radius of 2.23 m, supported by an extended structural framework. A cover gas envelops the upper surface of the water tank. The structural integrity of the OD lid is maintained by eight trusses, providing stability among the components. Together, these five essential elements—the water tank, ultra-pure water, cryostat, cover gas, and trusses—combine to

define the simulation geometry. It is crucial to emphasize that while all these components are considered in the simulation, the OD itself encompasses the tank, water, cover gas, and PMTs.

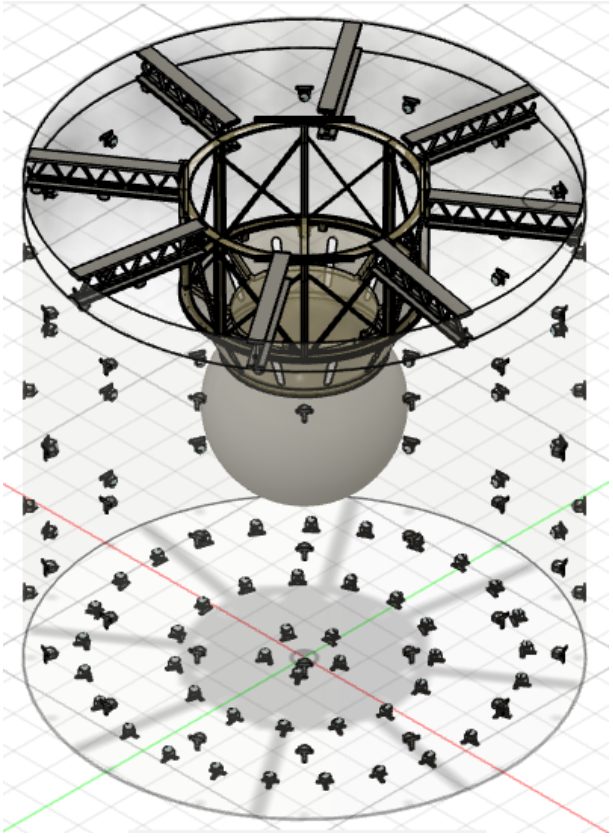

Figure 3.1 – The geometry of the OD is designed using the software tool Fusion 360. Key components, including the trusses that provide structural support, the cryostat, and the PMTs, are all displayed in this rendering. The center of the cryostat is defined as [0, 0, 0].

The OD cannot function as a Cherenkov detector without PMTs. A total of 125 PMTs are placed around the water tank in three main segments. On the side of the water tank, 64 PMTs are oriented inwards, organized into four rows and sixteen columns. These rows are positioned at distinct vertical (Z) coordinates, specifically at Z = -5.6 m, Z = -3.3 m, Z = -0.17 m, and Z = 3.5 m. On the floor of the water tank, 45 PMTs are installed to face upwards, arranged in three circular patterns at Z = -7 m. The outermost circle comprises 25 PMTs, the middle circle contains 15 PMTs, and the innermost circle accommodates 5 PMTs. Lastly, 16 PMTs are located on the upper surface of the water tank, just beneath

the cover gas on the trusses, facing downwards at Z = 4.5 m. Each truss supports 2 PMTs. The precise arrangement of these PMTs in the three segments is shown in Figure 3.2.

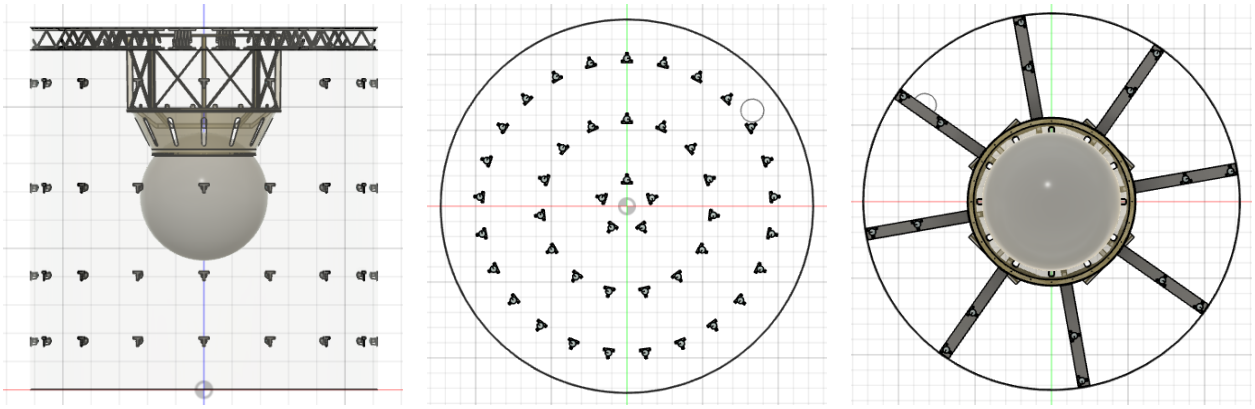

(a) **(b)** **(c)**

Figure 3.2 – A closer look at the locations of the PMTs on the (a) side, (b) floor and (c) top of the water tank.

The design of each of the PMTs in Fusion 360 mirrors the actual PMTs used in nEXO. Each PMT is composed of a metal T-shaped support structure, a glass housing, and a photosensitive photocathode. The photocathode has a hemispherical shape, and it plays the role of detection. Figure 3.3 illustrates the detailed design of a PMT within Fusion 360.

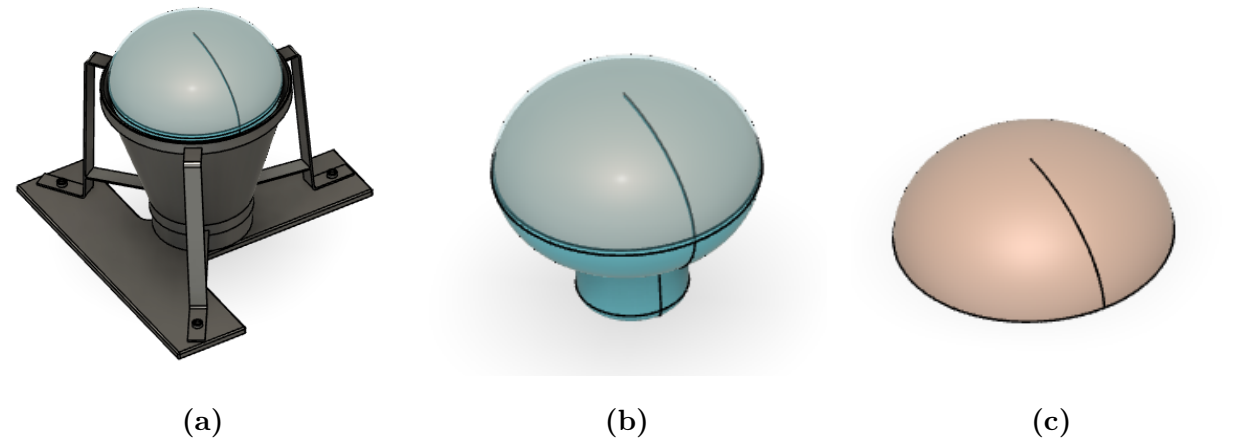

(a) **(b)** **(c)**

Figure 3.3 – The design of the PMTs in Fusion 360 encompasses (a) the complete assembly, (b) the glass housing, and (c) the photocathode, as illustrated.

To differentiate and identify the PMTs, a numbering system using PMT IDs is applied. Each PMT is assigned a unique number ranging from 0 to 124. This numbering system allows to study how many photons each PMT received in simulations. In the current geometry, the PMTs on the side are numbered from 0 to 63, starting from the lowest row and going up to the highest row. The PMTs on the floor are numbered from 64 to 108, arranged from the outer circle to the inner circle. Lastly, the PMTs on the top are numbered from 109 to 124, starting from the PMTs near the wall and proceeding towards the PMTs near the cryostat. This systematic numbering scheme enables efficient identification and analysis of the PMTs, contributing to the calibration process and providing insights into their light detection properties.

3.2 nEXO Outer Detector Calibration System

The calibration system designed for the nEXO OD is comprised of three main components: laser sources, optical fibers, and diffuser balls. The system operates as follows: The laser sources emit light, which is then transmitted through the optical fibers. This light is directed towards the diffuser balls, positioned within the water tank, and ultimately reaches all the PMTs, illuminating them. This straightforward design was chosen to ensure user-friendliness and easy maintenance of the calibration system.

3.2.1 Laser Sources

Laser sources serve as the light sources of the calibration system. To select a suitable laser source for integration into the calibration system, the first consideration is its wavelength. The laser sources' wavelength should fall within the range of the PMTs' maximum quantum efficiency. Quantum efficiency data for the Hamamatsu R5912 PMTs, the used PMTs in the OD of the nEXO experiment, was provided by the Daya Bay Reactor Neutrino Experiment [68] for 37 energy points ranging from 1.55 eV to 6.20 eV. Figure 3.4 illustrates the quantum efficiency as a function of photon energy for these 37 data points, along with the Gaussian approximation of the R5912 PMTs' quantum efficiency.

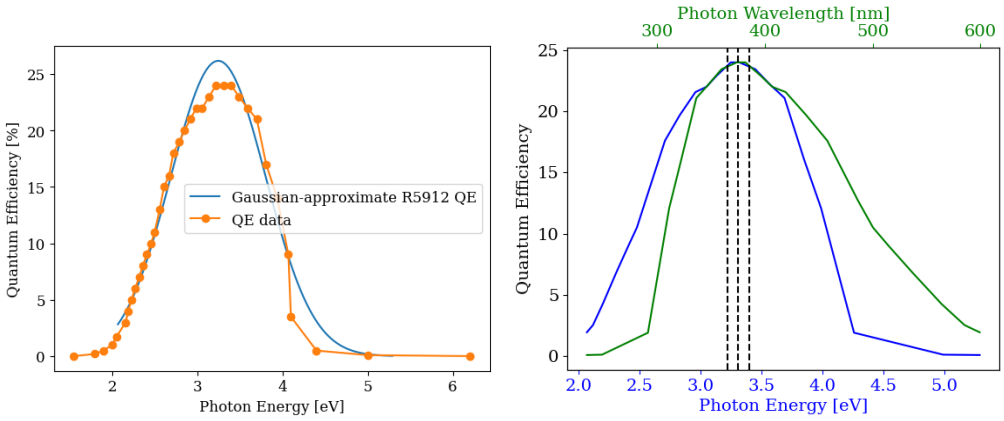

(a) **(b)**

Figure 3.4 – Quantum efficiency of the Daya Bay PMTs. (a) Measured data points are shown in orange while a Gaussian fit is shown in blue. (b) The blue curve shows quantum efficiency as a function of photon energy, while the green curve does the same for photon wavelength. The peak quantum efficiency, at 24%, is reached at photon energies of 3.22 eV, 3.31 eV, and 3.40 eV, corresponding to 385.31 nm, 374.84 nm, and 364.92 nm, respectively. These data points are denoted by dashed lines.

According to the datasheet of the PMTs [69], they exhibit a 25% quantum efficiency at 390 nm. Therefore, the data provided by Daya Bay is in good agreement with the datasheet information. However, this information alone is insufficient for making a decision. As discussed in chapter one, the OD functions as a Cherenkov detector, and therefore, the impact of Cherenkov radiation must also be taken into account to see at which wavelength the maximum number of photons is produced.

Cherenkov radiation refers to the emission of electromagnetic radiation when a charged particle, like an electron, moves through a dielectric medium at a speed surpassing the phase velocity of light in that particular medium. According to classical physics, when a charged particle accelerates, it emits electromagnetic waves. These waves form spherical wavefronts that propagate at the phase velocity of the medium (represented by the ratio of c to n, where c is the speed of light in vacuum and n is the refractive index of the medium). As the charged particle moves through the medium, the surrounding particles polarize in response to its presence. These polarized particles become excited by the charged particle, and upon

returning to their ground state, they re-emit the energy as photons. To generate Cherenkov radiation, the particle must surpass the phase velocity of light rather than the group velocity of light [70].

The Frank-Tamm formula, provides a tool to study the amount of emitted Cherenkov radiation [70]. This formula calculates the energy emitted by a charged particle per unit length and per unit of frequency. It is defined as follows:

$$\frac{\partial^2 E}{\partial x \partial \omega} = \frac{q^2}{4\pi}\mu(\omega)\omega(1 - \frac{c^2}{v^2 n^2(\omega)}). \tag{3.1}$$

The total amount of energy radiated per unit length can be written as:

$$\frac{dE}{dx} = \frac{q^2}{4\pi}\int \mu(\omega)\omega(1 - \frac{c^2}{v^2 n^2(\omega)})d\omega. \tag{3.2}$$

By solving the integration for frequency, we arrived at the following expression for calculating the total amount of energy radiated per unit length:

$$\frac{dE}{dx} = \frac{q^2}{4\pi}\mu(\omega)(1 - \frac{c^2}{v^2 n^2(\omega)})(\omega^2/2). \tag{3.3}$$

Here, q represents the electric charge of the particle. In the context of the nEXO OD, the Cherenkov radiation of muons is significant, and therefore, for our case, we have $q = -1 \times 1.6 \times 10^{-19}$ C. The variables $\mu(\omega)$ and $n(\omega)$ stand for the frequency-dependent permeability and index of refraction of the medium, respectively, and in our case, the medium is water, so $\mu(\omega) = -1.26 \times 10^{-6}$ [71]. The typical energy of a muon passing through water is about 300 GeV, corresponding to a velocity of approximately 1.58×10^8 m/s.

To calculate the total amount of emitted energy using the previously derived equation, a data set for the index of refraction at each energy point was required. This information was obtained by selecting a reference index of refraction for water [72]. Once all the variables were obtained, the total amount of energy and the total number of photons per millimeter were deduced.

The total photon count per millimeter using this approach is approximately 29, closely aligning with the Chroma [67] calculation (a fast optical Monte Carlo simulation with surface-

based geometries) on Wolfram Alpha [73] (an online computational knowledge engine), and the result reported in the reference [74]—all converging around 27 photons per millimeter.

As mentioned previously, the aim of this calculation is to find the wavelength at which the number of photons is maximum in order to choose a suitable laser source for the calibration system. The maximum quantum efficiency of the PMTs occurs at approximately 385 nm. However, after adding the effect of Cherenkov radiation, the maximum number of detected photons occurs at approximately 360 nm, resulting in a slight shift to lower wavelengths. This fact is visually represented in Figure 3.5. The next consideration is whether the variation in wavelengths affects the intensity needed for the calibration system. This will be examined as the intensity equation is discussed.

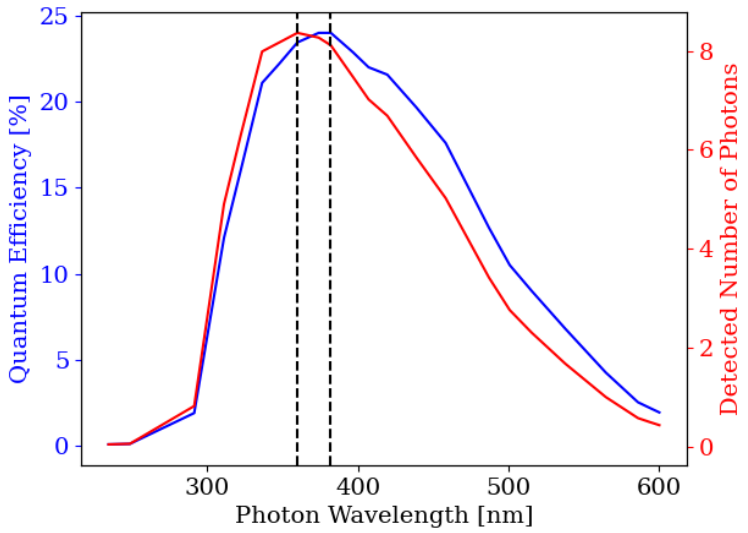

Figure 3.5 – The shift in wavelength occurs as a result of adding the effect of Cherenkov radiation.

The intensity of the laser source is another property that requires careful consideration for the calibration system. In this context, intensity refers to the number of photons emitted by the laser. Ensuring an appropriate intensity level is essential, as the calibration process relies on the PMTs receiving an adequate number of photons. On one hand, the intensity of the laser source must not fall below a specific threshold, as doing so would result in PMTs not receiving the required number of photons for proper calibration. This number is determined based on the trigger condition of the PMTs. On the other hand, it is important not to

excessively increase the laser source intensity, as there exists a threshold beyond which the PMTs would become saturated. When only a few photons are received, the output charge of a PMT increases in direct proportion to the number of detected photons. However, when there is a high influx of photons, the PMT's linear response deteriorates, leading to saturation. Such saturation could lead to erroneous responses from the PMTs to the incoming photon levels.

The intensity at which the PMTs become saturated depends on the characteristics of the PMT. While the datasheet of the Hamamatsu R5912 PMTs does not provide direct information on the saturation limit, we can calculate it based on the parameters described in the datasheet. Two parameters for this calculation are the anode current (I_A) and gain (G).

Anode current refers to the average electric current that flows through the PMT's anode (output) over a specific time period. It measures the number of photoelectrons emitted by the photocathode. In our case, the anode current is 0.1 mA. Gain represents the average number of electrons emitted by the PMT for each incident photon on the photocathode. In our case, the gain is 10^7. We can calculate the average number of incident photons that result in a specific number of electrons, typically referred to as the photon-to-electron conversion. This calculation involves first determining the number of electrons resulting from the anode current and then dividing that value by the gain

$$N_e = 10^{-4}A/1.6 \times 10^{-19}C \sim 10^{14}) \tag{3.4}$$

$$N_p = 10^{14}/10^7 \sim 10^7. \tag{3.5}$$

After considering the quantum efficiency of the PMTs, the resulting number is 2.5 million photons. This indicates that the PMTs maintain linear behavior until they receive more than 2.5 million photons per second. This is also evident in Figure 3.6.

To determine the intensity levels at various distances from the diffuser ball, the following method is employed. The available surface area for each PMT capable of detection, denoted as A_{PMT}, is calculated as $A_{PMT} = \pi r^2$, where r represents the PMT radius, which measures 10.16 cm (4 inches). The total surface area, A_{total}, is defined as $A_{total} = 4\pi D^2$, with D

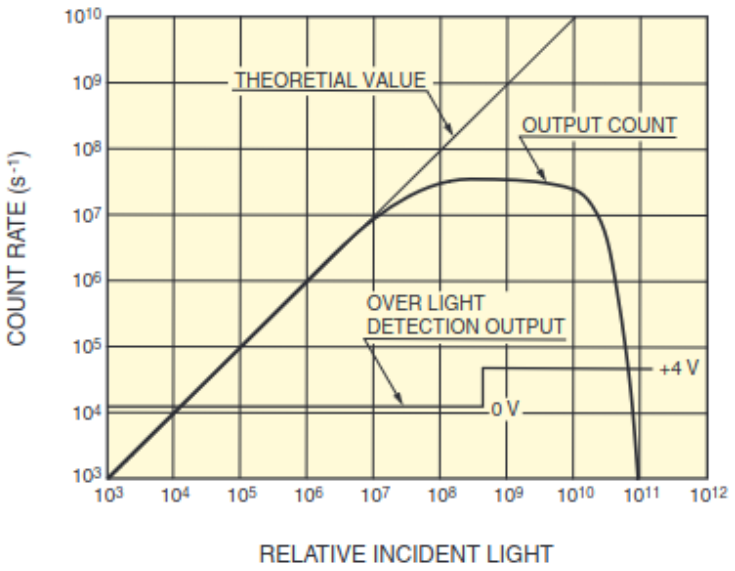

Figure 3.6 – When photons continously enter PMTs at intervals matching its pulse-pair resolution, it is theoretically possible to measure photons up to the reciprocal of this resolution. However, beyond a certain light intensity threshold, the count value no longer correlates proportionally with the light level. The figure originates from [75].

signifying the distance between the diffuser ball and the PMT. The fraction of photons reaching a PMT is expressed as

$$I = I_0 \cdot \frac{A_{PMT}}{A_{total}} = I_0 \cdot \frac{r^2}{4D^2}. \tag{3.6}$$

Two additional factors significantly influence the number of photons detected by a PMT: the PMT's quantum efficiency and water attenuation. The influence of quantum efficiency is incorporated by multiplying the equation by ϵ, representing the quantum efficiency of the PMTs, which we have established to be $\epsilon = 25\%$. The impact of water scattering and absorption at the distance D under uniform attenuation conditions, is accounted for by multiplying the equation by $e^{-\mu D}$, where μ is the attenuation coefficient (the sum of absorption and scattering coefficients). This coefficient quantifies the rate at which the intensity of a beam diminishes as it propagates through a material. The resulting equation captures the intensity received by a PMT, taking into account all relevant contributing

parameters

$$I = I_0 \cdot \frac{r^2 e^{-\mu D} \epsilon}{4D^2}. \tag{3.7}$$

In this equation, I_0 represents the initial intensity required for calibrating the designated PMT. I denotes the intensity needed at the location of the PMT. For our experimental setup, we have decided to set a value of 10, ensuring that each PMT receives a minimum of 10 photons during the calibration process.

The variables I, r, and ϵ are considered constant. Additionally, for a specific diffuser ball location, the distance between the diffuser ball and the PMTs remains constant. Therefore, when investigating the impact of using different laser sources with varying wavelengths, the sole parameter that requires examination is the attenuation coefficient. To investigate this effect, a location for the diffuser ball was selected and the distance between the diffuser ball and all the PMTs was measured. The attenuation coefficient at each wavelength was determined based on data from the paper "The Optical Properties of Pure Water" [76]. The results have been illustrated in Figure 3.7.

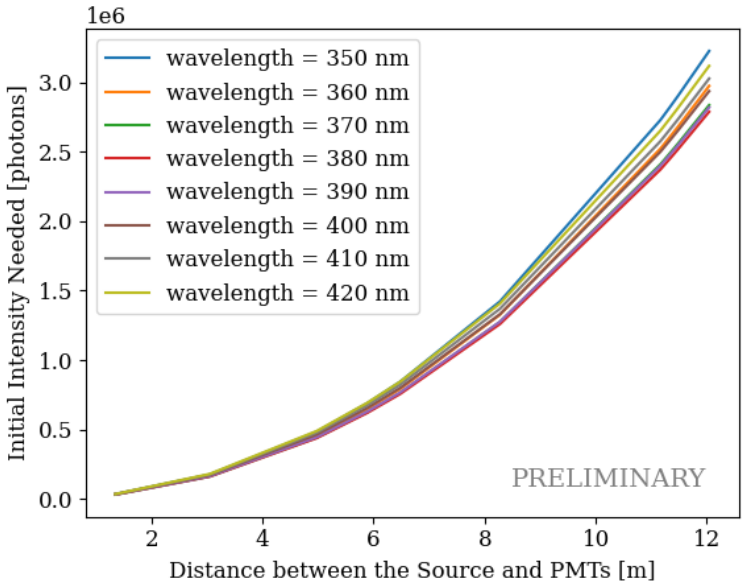

Figure 3.7 – The impact of laser source wavelengths on the initial intensity required for PMT calibration assuming that the diffuser ball is located in the middle of the floor of the water tank. Even at a distance of 12 m, the dimension of the water tank, there is only 10-15% reduction due to attenuation at different wavelengths.

Figure 3.7 demonstrates that the variation in using different wavelengths becomes significant only at considerable distances between the diffuser ball and the PMTs. Specifically, the effect becomes apparent when a PMT is situated more than 8 meters away from the diffuser ball. In the forthcoming sections, I will discuss the necessity of employing multiple diffuser balls for the calibration system. Based on this fact, the crucial aspect that should be considered for the wavelength selection is to maximize the number of detected photons. Considering this, laser sources with wavelengths ranging from 360 nm to 390 nm are recommended.

3.2.2 Diffuser Balls

A diffuser ball is a spherical or ball-shaped device designed to scatter light in multiple directions. It is supposed to emit a uniform and homogeneous lighting. Typically crafted from translucent or semi-translucent materials, the diffuser ball enables light to disperse in various directions as it passes through its surface. This scattering effect occurs due to the presence of random microscopic irregularities on the material's surface.

In the context of the calibration system, the quantity and positioning of diffuser balls are important. The placement of these diffuser balls ensures the even distribution of light throughout the system. Furthermore, determining the appropriate number of diffuser balls is required for achieving the desired light scattering properties necessary for the calibration process.

The first question regarding the diffuser balls is determining the required quantity. The answer to this question heavily depends on the geometry of the OD and the locations of the PMTs within the system. A crucial tool in making this determination is the light map of the OD. The light map provides a comprehensive understanding of light propagation and interactions within the water tank, offering insights into the distribution and intensity of light across various regions. By analyzing the information derived from the light map, we can make informed decisions regarding the optimal number and strategic placement of diffuser balls.

Figure 3.8 displays four distinct light maps of the OD, each corresponding to a specific diffuser ball location. All four light maps were simulated with a total initial photon count

of one million. The light map analysis considers the paths and positions of photons as they interact and propagate through the water tank and detector components. All the light maps used in this study were generated using the Chroma [67] simulation software. The output of the Chroma simulation provides a light map, which is divided into three main segments, each representing one part of the OD: top, side, and bottom.

Through simulations and analyses, it becomes evident that a single diffuser ball cannot adequately address the calibration photon requirements for all PMTs. Even with variations in the diffuser ball's position and the number of photons generated, some PMTs may not meet the minimum calibration requirement of receiving at least 10 photons, as mandated by the trigger condition. This limitation is primarily due to the geometry of the OD and the presence of the shadow cast by the cryostat on the PMTs located behind it. The best outcome observed in the light maps occurs when the diffuser ball is positioned at the center of the floor, seemingly eliminating the cryostat shadow. However, even in this scenario, PMTs located at the top of the detector fail to receive the appropriate number of photons needed for calibration.

Based on the analysis, it is indeed possible to illuminate all the PMTs using two or three diffuser balls. However, it is important to consider that achieving this illumination requires an extremely high initial intensity of light. Such high intensity levels pose a challenge, as the PMTs closest to the diffuser ball may receive an excessive number of photons at once, leading to saturation. This saturation can make it difficult to calibrate them accurately.

To address this issue, a pragmatic choice is to use four to five diffuser balls. This option allows for a more balanced distribution of light and ensuring a more controlled photon count for each PMT during calibration. Employing five diffuser balls effectively means having approximately one diffuser ball for every 25 PMTs. This approach proves especially useful when specific groups of PMTs need calibration. The distribution of diffuser balls allows for targeted calibration of specific regions, optimizing the calibration process and achieving precise results for different PMT groups. Ultimately, the decision to use multiple diffuser balls strikes a balance between achieving uniform illumination across PMTs while avoiding issues related to excessive photon intensity.

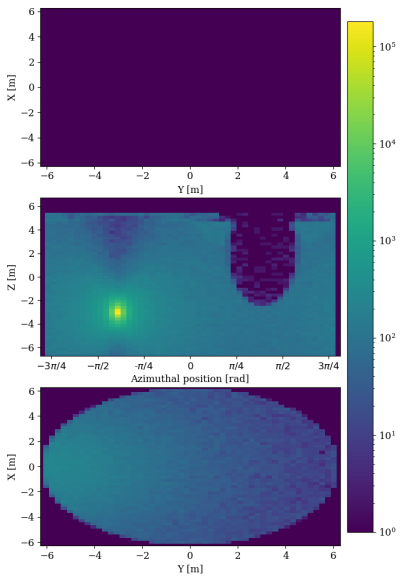

(a) Diffuser ball at [0, -3, -6] m

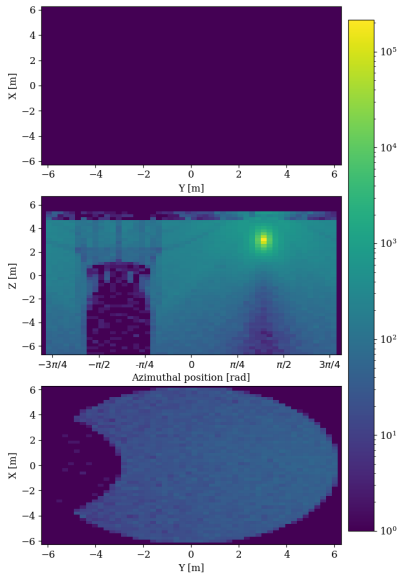

(b) Diffuser ball at [0, 3, 6] m

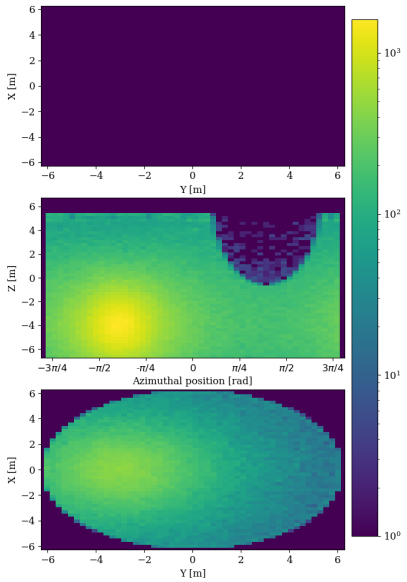

(c) Diffuser ball at [0, -3, -4] m

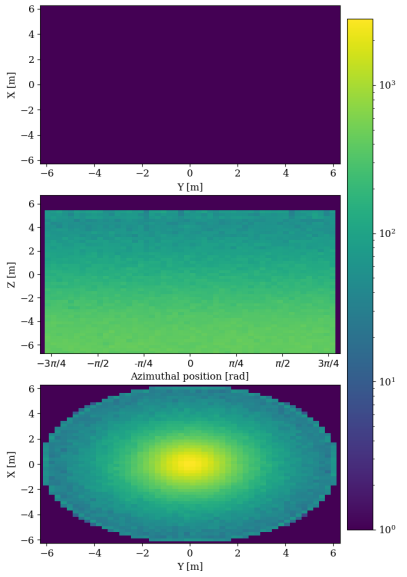

(d) Diffuser ball at [0, 0, -6] m

Figure 3.8 – The light map of the OD. The brightest point on the image corresponds to the position of the diffuser ball.

With the number of diffuser balls defined, the next step is determining their placement. To ensure a streamlined installation process and to minimize unnecessary additions to the OD medium, an essential criterion must be met: the diffuser balls can only be affixed to a surface. As a result, suspending them in the middle of the water tank, which would necessitate structural support, is unfeasible. Instead, the attachment of diffuser balls is confined to the tank's walls, floor, or ceiling.

The placement of diffuser balls offers various possibilities, each with unique implications. Analyzing the light map data reveals a promising option: positioning a diffuser ball at the bottom center of the water tank to promote even photon distribution. An extension of this idea involves placing four additional diffuser balls on the left and right tank walls, each at slightly different heights. Chapter four will investigate the effectiveness of this configuration and its impact on the system's overall performance.

3.2.3 Optical Fibres

Optical fibers are used in a variety of applications such as in telecommunications for transmitting information in the form of light pulses over long distances. Fibers are composed of thin strands made of either glass or plastic, designed to guide and transmit light signals through their core using the principle of total internal reflection. The use of optical fibers provides several advantages, including low signal loss over long distances, high bandwidth capabilities, and immunity to electromagnetic interference.

In our system, optical fibers transmit light from laser sources outside of the tank to the diffuser balls located inside the water tank. By efficiently guiding the light signals, optical fibers ensure that the illumination from the laser sources effectively reaches the diffuser balls, facilitating uniform scattering of light within the water tank.

To carry a large number of photons in a calibration system for PMTs inside a water tank, an optical fiber that offers high efficiency in transmitting light and low signal attenuation is needed. The choice of optical fiber will depend on factors such as the wavelength of the photons, the distance they need to travel, and the requirements of the calibration system.

In our scenario, the most suitable type of optical fiber would be a low-loss, high-NA (numerical aperture) multimode fiber or a specialty optical fiber designed for high transmission

efficiency. High-NA multimode fibers have a larger core size, which allows them to accept a broader range of light angles, increasing their light-gathering capability. Given the large distance, it is crucial to account for signal loss due to attenuation, scattering, and other environmental factors that could affect the performance of the fiber.

— Single-Mode Fiber (SMF): If the distance between the source and the diffuser ball is indeed long, single-mode fibers should be considered. The standard attenuation values for intrinsic losses in single-mode fibers are roughly 0.40 dB/km at 1310 nm and 0.30 dB/km at 1550 nm.

— Photonic Crystal Fiber (PCF) with High-NA: PCFs with high numerical aperture can be designed to have low-loss transmission at specific wavelengths. These fibers can handle a large number of photons efficiently and may be suitable for both short and long-distance applications.

— Specialty UV-Enhanced Fiber: For UV applications like at 380 nm, some optical fiber manufacturers offer specialty UV-enhanced fibers designed to maximize transmission efficiency at UV wavelengths.

In this chapter, we have gained a comprehensive overview of the properties inherent to the components of the calibration system. These properties encompass critical factors such as radiant sensitivity and intensity requirements, which collectively contribute to the calibration process's precision and reliability. By understanding the spectral response characteristics of the PMTs, as well as the principles guiding the utilization of diffuser balls, we have established a foundation for the subsequent steps.

The forthcoming chapter is poised to delve deeper into the practical implementation and outcomes of the calibration system. Through the application of Chroma [67] simulations, we will be able to showcase the real-world results achieved by employing this setup.

Chapter 4

The nEXO Outer Detector Calibration System through the Lens of Chroma Simulation

With the design consideration of the calibration system outlined, the focus now shifts towards practical validation. To comprehensively understand how this system operates and its potential impact, the simulation of its functionality becomes imperative. For this purpose, Chroma simulations were used.

4.1 Chroma Simulation

After establishing the design of the calibration system, it is now essential to delve into the practical functioning of this system. One effective approach to comprehensively assess its efficacy is through simulating its application. The entire analysis pertaining to the calibration system of the nEXO OD was conducted exclusively through the utilization of the Chroma simulation [67] framework. To validate the integrity and accuracy of the obtained results, a comparative analysis was performed between the outcomes derived from the Chroma simulation and those obtained from the GEANT4 [77] simulation.

The availability of high-speed workstations and extensive computing clusters has elevated the utility of Monte Carlo simulation throughout the various stages of experiment design

and data interpretation within the field of particle physics. Libraries such as GEANT4 have established a shared framework for generating simulations based on particles, which has been embraced by numerous recent undertakings in high-energy and nuclear physics research. After years of extensive refinement and with a substantial user base, GEANT4 offers a wide array of features, many of which have undergone rigorous validation using real detector data. One of the pivotal choices within the GEANT4 framework revolves around the depiction of detector geometry. Specifically, a detector is represented as a hierarchical arrangement of nested solids, each characterized by a particular material and mathematically encoded through a designated C++ [78] class [67].

An alternative approach to the conventional paradigm becomes feasible through the introduction of an alternate perspective: depicting a detector as an arrangement of oriented triangles that represent the interfaces between the distinct materials constituting both the "interior" and "exterior" of the detector. Specifically, for the task of efficiently propagating optical photons within a substantial detector, the surface-based methodology has the potential to achieve significantly enhanced speed and seamless parallelization. This is particularly evident on the increasingly ubiquitous graphics processing units (GPUs). Chroma is the software implementation of this innovative approach [67].

The structure of the surface-based detector model is exclusively composed of repetitive triangular patches, which extensively cover the surfaces delineating various volumes. These triangles are equipped with material codes and distinctive identification numbers, facilitating their correlation with specific objects of interest, such as particular PMTs. This type of detector model, which is based on surfaces, accepts a trade-off in precision when representing curved surfaces in exchange for the significant optimization potential in tracking particle paths. However, the degree of approximation is modifiable by diminishing the dimensions of the triangular patches used to chart the surface characteristics of the object [67].

In the context of reconstructing data, the utilization of a ray-tracing technique and the detailed tracking of individual photon trajectories are unnecessary. Instead, the Chroma focus lies in capturing the photons that register hits on PMTs and generating a probability density function (PDF) for timing across numerous events. This timing PDF becomes a crucial element in evaluating the likelihood function. This operation involves identifying the

detected photons, applying the timing response of the PMTs, and subsequently determining the earliest recorded time of impact (if any) for each unique PMT identification in the event [67].

At present, Chroma has achieved the capability to model around one million photons per second within a water Cherenkov detector. This simulation encompasses various physics phenomena, including absorption, Rayleigh scattering, Fresnel reflections, and refraction. The tool is also serving a role in aiding the refinement of a Monte Carlo-driven maximum likelihood reconstruction algorithm [67].

4.2 Chroma Simulation Launch

A preliminary step preceding the simulation is the examination of the optical characteristics inherent to all components housed within the water tank. This entails a comprehensive assessment to discern the appropriate optical properties for each component, specifically focusing on absorption and scattering lengths. Of particular significance in our endeavor was the evaluation of these properties for the tank's walls.

The walls of the tank were designated as fully absorptive surfaces. This choice is rooted in the objective of excluding photons that might reflected the walls and subsequently be detected by a PMT. By opting for complete absorptance, we effectively narrow the focus of this study to photons that, immediately upon emission from the diffuser balls, proceed to the PMTs and allows us to exclusively analyze the photons that reach the PMTs without any interaction. The optical properties of the stainless steel walls and outer cryostat surface are summarized in Table 4.1.

Table 4.1 – The optical properties of the components in the Chroma.

Component	**Specular Reflectivity**	**Absorption**	**Diffuse Reflectivity**
Stainless steel	0.00	1.00	0.05
Outer cryostat surface	0.98	0.02	0.00

The next step involves selecting the appropriate photon generator. In our particular scenario, the light generators are diffuser balls situated within the water tank. These diffuser balls are adept at scattering light in all directions. Among the various generator options

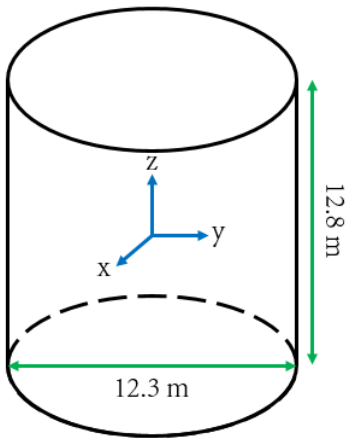

Figure 4.1 – A schematic of the OD to show the coordinates system in the Chroma simulation.

available in the Chroma, the most optimal choice is the utilization of a photon bomb. This photon bomb effectively mimics the behavior of a diffuser ball within the confines of the water tank. This choice ensures that the emitted light undergoes scattering akin to what would occur with a diffuser ball setup. The wavelength of the generated photons is set to 390 nm.

Moving on to the third step, the precise placement of our diffuser balls demands attention. As elucidated in chapter three, our strategy involves incorporating a total of five diffuser balls. One of these diffuser balls will be positioned at the center of the water tank's floor, forming a focal point. Furthermore, an arrangement of four additional diffuser balls will be established along both the left and right walls of the tank.

Assuming a cylindrical shape for the water tank, with a radius of 12.3 m and a height of 12.8 m as depicted in Figure 4.1, the coordinated configuration within the Chroma simulation for the nEXO OD is as follows: The x-coordinate depicts forward-backward motion and covers a span from -6150 mm to 6150 mm. The y-coordinate denotes left-right variations and spans a range of -6150 mm to 6150 mm. Finally, the z-coordinate indicates vertical positioning within the water tank's height dimension, which extends from -7000 mm to 5800 m m, accommodating both upward and downward movements.

Positioning the first diffuser ball at the central point of the water tank's floor is achieved by utilizing the coordinates [0, 0, -7038] mm. This positioning holds particular significance due to its alignment with the z-coordinate value that corresponds to the vertical placement of the PMTs on the floor of the tank. By being situated at the same z-coordinate level as the PMTs, the diffuser ball becomes a source of illumination for a subset of PMTs positioned on the tank's floor. Furthermore, this diffuser ball's emitted light also reaches a portion of the PMTs situated on the first row at the lowest side.

The subsequent disposition of the remaining four diffuser balls is distributed on the walls. One is placed at [0, -6000, -4433.5] mm, between the first two bottommost rows of PMTs on the tank's side. Positioned at these coordinates, it illuminates PMTs on the left-hand section of these two rows. The other one is placed at [0, -6000, 1678.5] mm. Similar to the other diffuser ball, this one is positioned on the left wall, specifically between the third and fourth rows of PMTs. Its coordinates facilitate the illumination of the left-side PMTs within these two rows.

The final two diffuser balls are positioned along the right wall of the water tank. One is placed at [0, 6000, -1721] mm, between the second and third rows of PMTs on the side. The remaining diffuser ball is situated at coordinates [0, 6000, 3082] mm, positioned between the last row of PMTs on the side and the ceiling of the tank. This placement serves the purpose of illuminating the PMTs located on the highest part of the water tank, as well as the PMTs on the trusses.

Through the arrangement of these diffuser balls, we ensure coverage of photon illumination across all PMTs within the water tank. This placement guarantees that every PMT, regardless of its location, receives the necessary exposure to photons emitted from the diffuser balls. To visualize the functionality of these placements, photon path plots come in handy.

While the light maps were instrumental in addressing the question of how many diffuser balls are required (chapter three), the photon path plots serve a role in determining the location of the diffuser balls. The photon path plots provide insights into the trajectories of individual photons within the system. These plots offer an understanding of where the diffuser ball is situated, as they display the initial points of photons generated by the diffuser

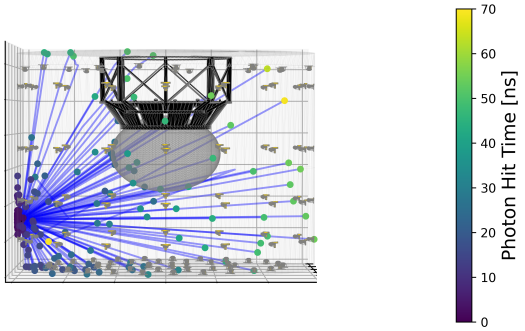

(a) Diffuser ball located at [0, -6000, -4435.5] mm

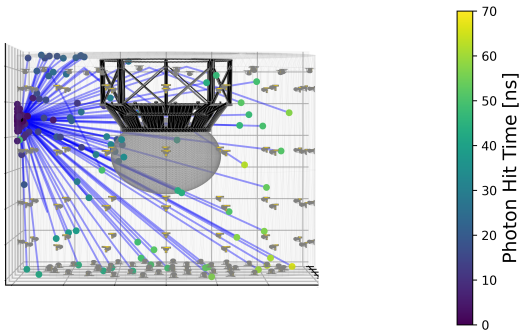

(b) Diffuser ball located at [0, -6000, 1678.5] mm

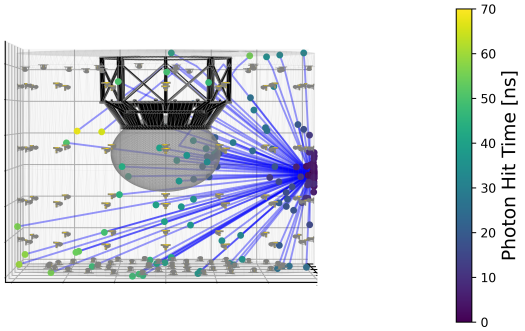

(c) Diffuser ball located at [0, 6000, 1721] mm

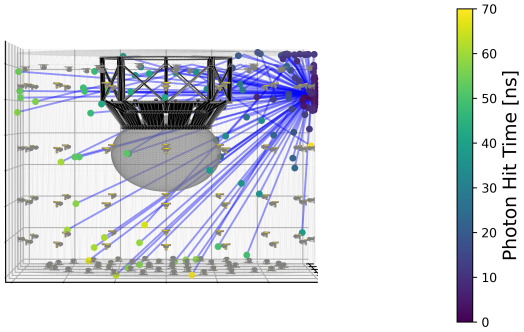

(d) Diffuser ball located at [0, 6000, 3082] mm

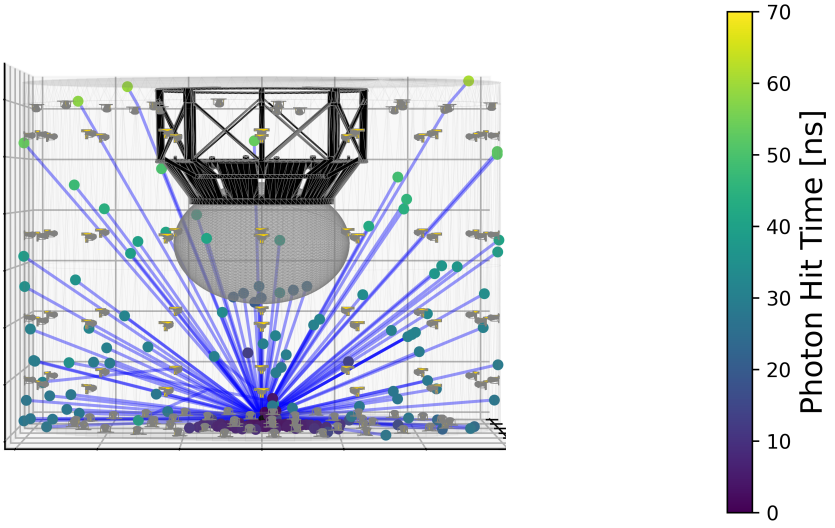

(e) Diffuser ball located at [0, 0, -7038] mm

Figure 4.2 – The photon path plots for the diffuser balls located at locations indicated in the subcaptions.

ball. Additionally, these plots show the final points where these photons are detected after traversing through the water tank and interacting with the PMTs. Furthermore, the photon path plots present the photon hit time, which is useful for studying the timing properties of the PMTs' readout system.

4.3 Final Analysis

The final step involves determining the intensity at each respective diffuser ball location. As detailed in chapter three, we formulated an equation that takes into account all the parameters influencing the calibration process (Equation 3.7). This equation serves the purpose of calculating the initial intensity necessary for calibrating the PMTs. Equation 3.7 can be expressed as follows:

$$I_0 = I \cdot \frac{4D^2 e^{\mu D}}{r^2 \epsilon}. \tag{4.1}$$

The practical procedure entails the selection of a location for the diffuser ball. Subsequently, by employing the equation and interpreting the resultant plot, one can readily acquire the required intensity value I_0.

Upon examining the plots (Figure 4.3), a clear pattern emerges. Specifically, when an intensity of two million photons is generated, it becomes evident that the PMTs located in close proximity to the diffuser balls, spanning distances of up to 10 meters, effectively capture the necessary photon count for the calibration process without becoming over saturated. The maximum number of photons received by an individual PMT will not exceed 2000 photons, while saturation occurs when a PMT receives more than 2.5 million photons per second. Emitting an intensity of 2 million photons ensures that the PMTs consistently collect the required quantity of photons. A light source operating at a wavelength of 390 nm, with the capability to emit 2 million photons within a 10 ns timeframe, should possess a power output of approximately 50 nW. This power level is relatively low when compared to existing light sources. As a result, achieving the desired initial intensity of 2 million photons is possible using currently available light sources.

In the conclusive segment of this study, an assessment entails gauging the efficacy of the established configuration. This evaluation hinges upon analysis of the results derived from

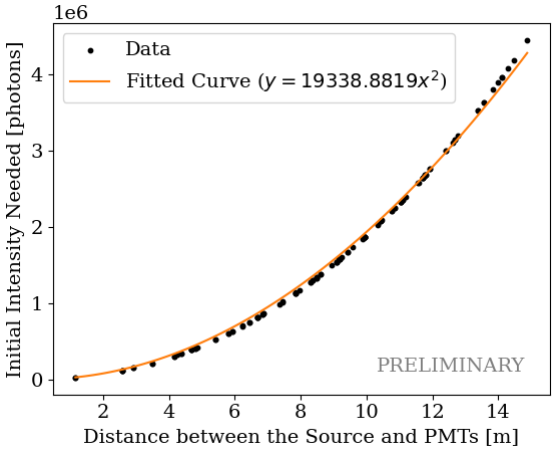

(a) Diffuser ball at [0, -6000, -4433.5] mm

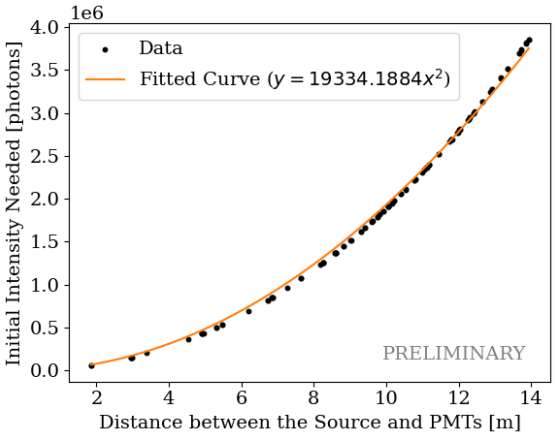

(b) Diffuser ball at [0, -6000, 1678.5] mm

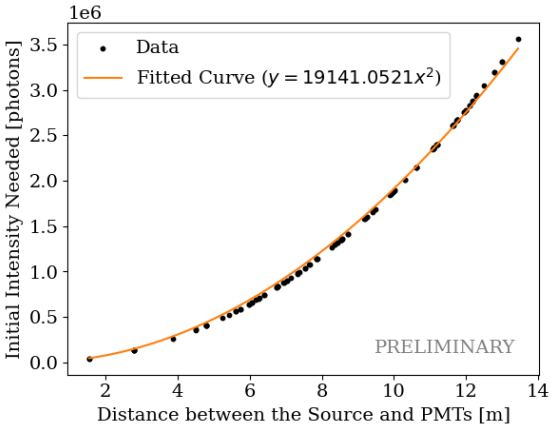

(c) Diffuser ball at [0, 6000, -1721] mm

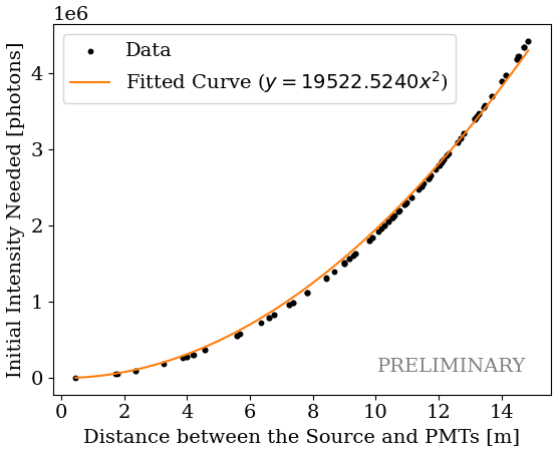

(d) Diffuser ball at [0, 6000, 3082] mm

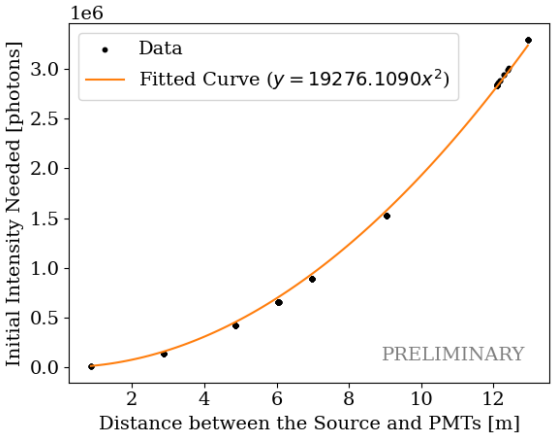

(e) Diffuser ball at [0, 0, -7038] mm

Figure 4.3 – The initial intensity plots for diffuser balls positioned at various locations. Plotted is the analytical data, based on Equation 4.1, which shows the initial intensity required at each PMT location as a function of the distance between the diffuser ball and the PMT.

employing the devised system. To this end, the outcomes from the Chroma simulation have been instrumental. In particular, the tagging function within the simulation framework has proven invaluable for discerning the photon distribution across various Channel IDs (PMTs). Table 4.2 provides an overview of the key properties defining the simulation setup.

Table 4.2 – Simulation parameters and corresponding settings.

Parameter	**Setting**
Generator	PhotonBomb
Photon wavelength	390 nm
Number of photons	2,000,000

The forthcoming section proceeds by presenting a pair of plots for each individual diffuser ball (Figures 4.4 to 4.8). Firstly, a scatter plot is presented, providing a visual representation of whether PMTs situated within a 10-meter radius from the diffuser ball have successfully received the required photon count. Additionally, a bar plot is included, serving as a comparative visualization of the photon distribution among different Channel IDs. By combining the insights from both the scatter and bar plots, we can assess the situation. This methodical analysis helps us thoroughly evaluate the configuration's feasibility and effectiveness. Using this approach, the study leads to a well-supported conclusion about the successful implementation and performance of the proposed system configuration. Additionally, Figure 4.9 provides an overview of the calibration system's operation.

In chapter three, it was mentioned that the threshold for PMTs is 2.5 million photons per second. We can specify that during calibration, the maximum number of photons a PMT can receive should not exceed 50. Figures 4.10 to 4.14 have been designed to illustrate this specific scenario, where PMTs that can be calibrated by a particular diffuser ball are highlighted in yellow.

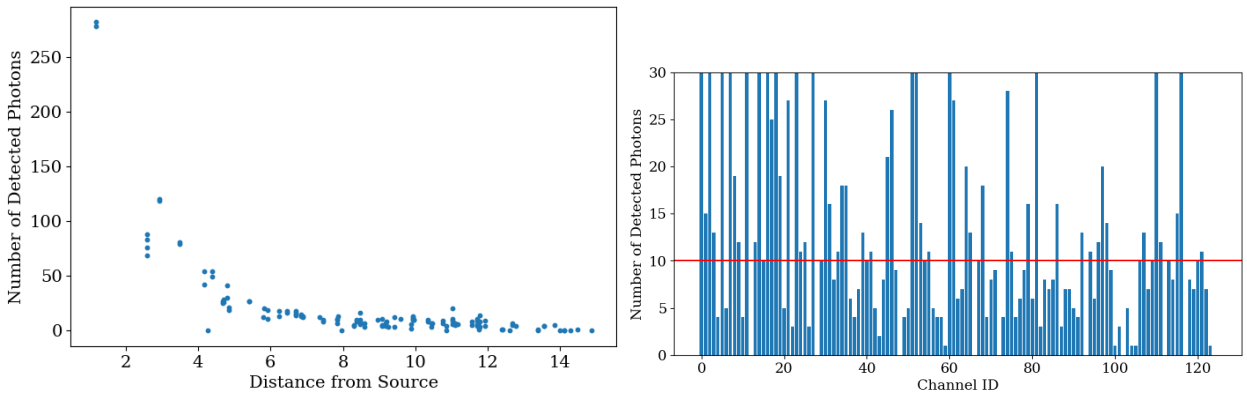

(a) **(b)**

Figure 4.4 – The scatter plot (a) and bar plot (b) illustrate the simulated data for a ball location of [0, -6000, -4433.5] mm. The scatter plot presents the number of detected photons as a function of the distance between the diffuser ball and the PMT and the bar plot indicates the number of detected photons for each channel (PMT). The red line on the bar plot indicates the 10 photon detection requirement.

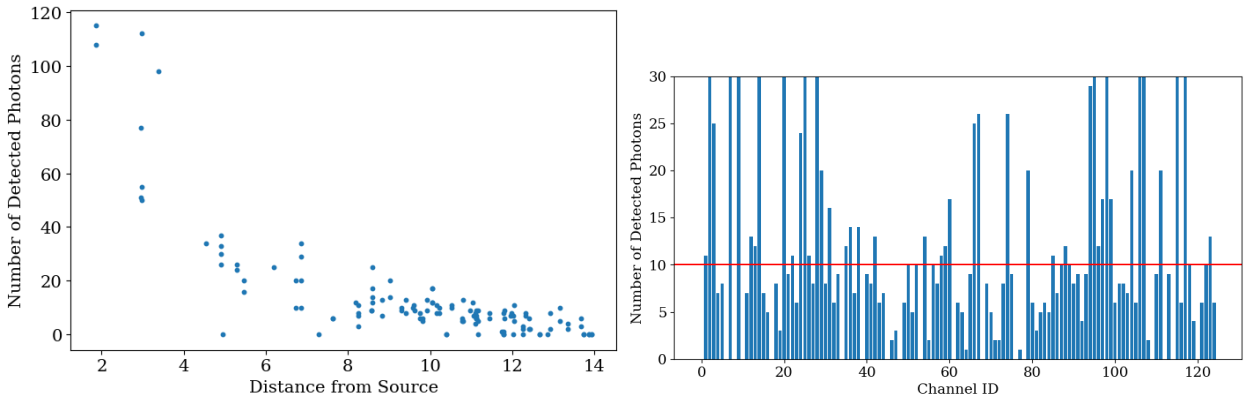

(a) **(b)**

Figure 4.5 – The scatter plot (a) and bar plot (b) illustrate the simulated data for a ball location of [0, -6000, 1678.5] mm. The scatter plot presents the number of detected photons as a function of the distance between the diffuser ball and the PMT and the bar plot indicates the number of detected photons for each channel (PMT). The red line on the bar plot indicates the 10 photon detection requirement.

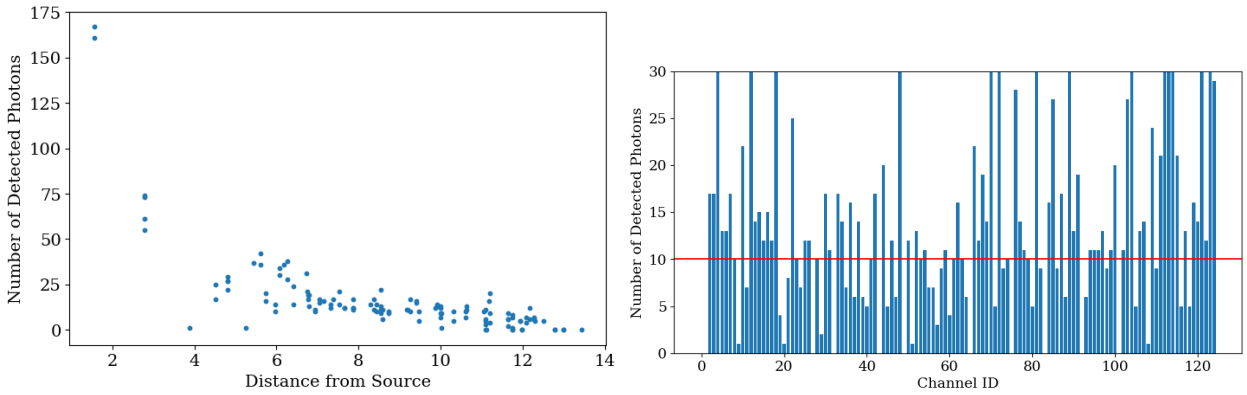

(a) **(b)**

Figure 4.6 – The scatter plot (a) and bar plot (b) illustrate the simulated data for a ball location of [0, 6000, -1721] mm. The scatter plot presents the number of detected photons as a function of the distance between the diffuser ball and the PMT and the bar plot indicates the number of detected photons for each channel (PMT). The red line on the bar plot indicates the 10 photon detection requirement.

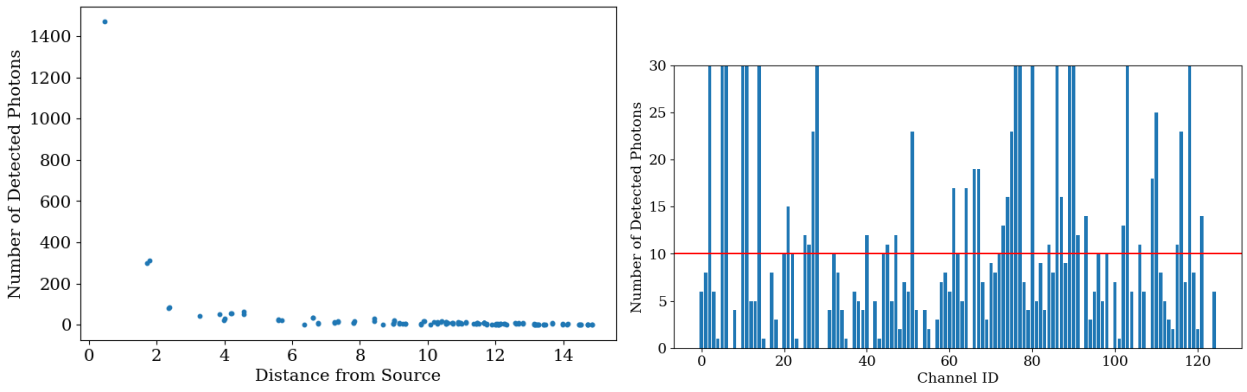

(a) **(b)**

Figure 4.7 – The scatter plot (a) and bar plot (b) illustrate the simulated data for a ball location of [0, 6000, 3082] mm. The scatter plot presents the number of detected photons as a function of the distance between the diffuser ball and the PMT and the bar plot indicates the number of detected photons for each channel (PMT). The red line on the bar plot indicates the 10 photon detection requirement.

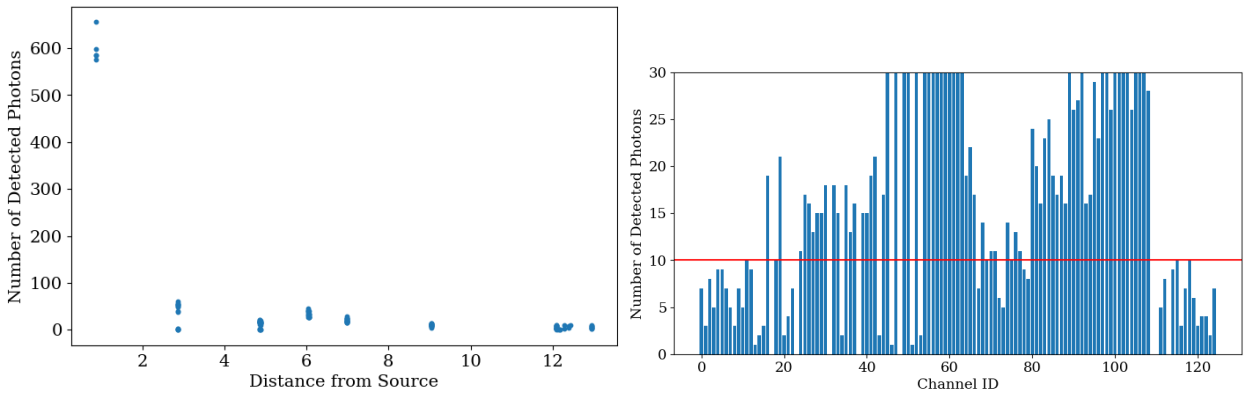

(a) (b)

Figure 4.8 – The scatter plot (a) and bar plot (b) illustrate the simulated data for a ball location of [0, 0, -7038] mm. The scatter plot presents the number of detected photons as a function of the distance between the diffuser ball and the PMT and the bar plot indicates the number of detected photons for each channel (PMT). The red line on the bar plot indicates the 10 photon detection requirement.

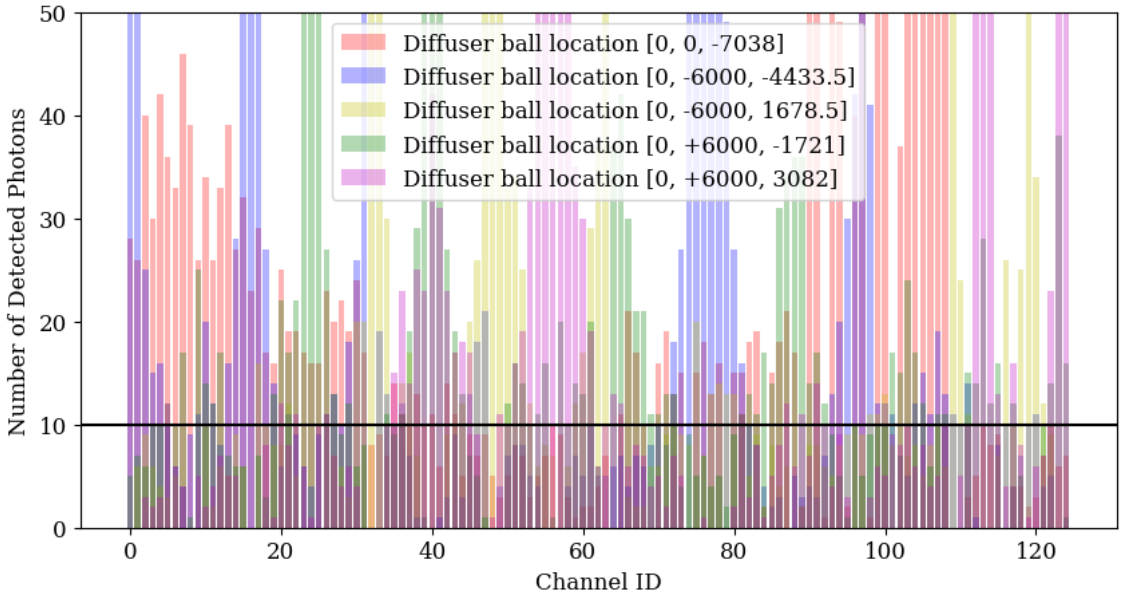

Figure 4.9 – The plot depicts the photon count received by each PMT when utilizing various diffuser balls, each represented by a color. The visual evidence indicates that employing the mentioned configuration ensures that all PMTs receive the requisite amount of photons.

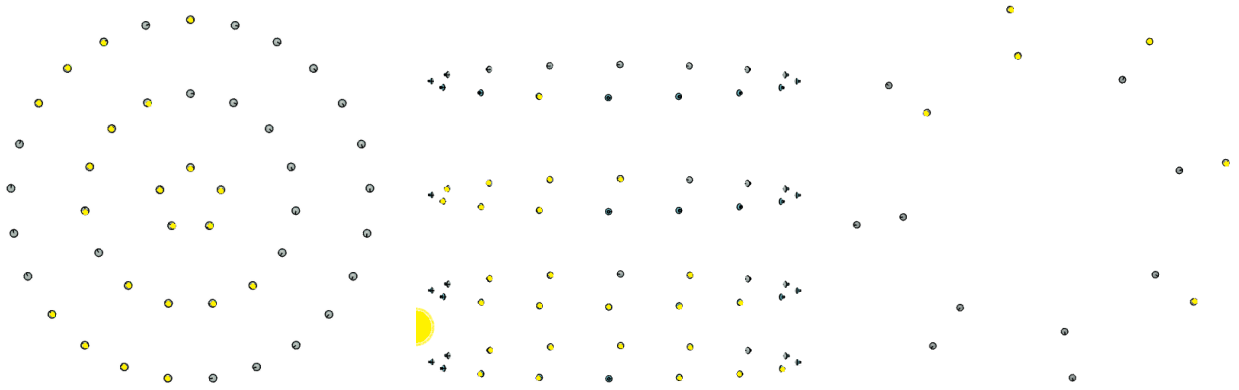

(a) Floor **(b)** Side **(c)** Top

Figure 4.10 – The PMTs highlighted in yellow can be calibrated using the diffuser ball located at coordinates [0, -6000, -4435.5] mm.

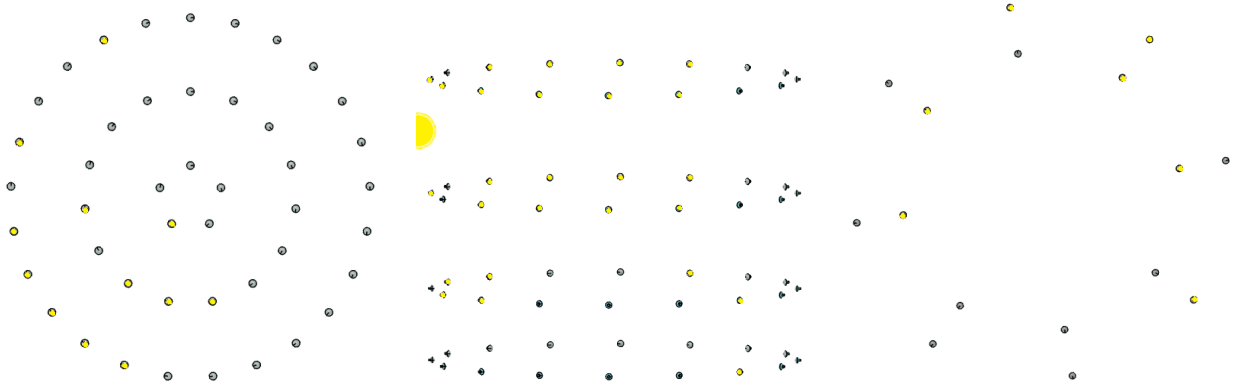

(a) Floor **(b)** Side **(c)** Top

Figure 4.11 – The PMTs highlighted in yellow can be calibrated using the diffuser ball located at coordinates [0, -6000, 1678.5] mm.

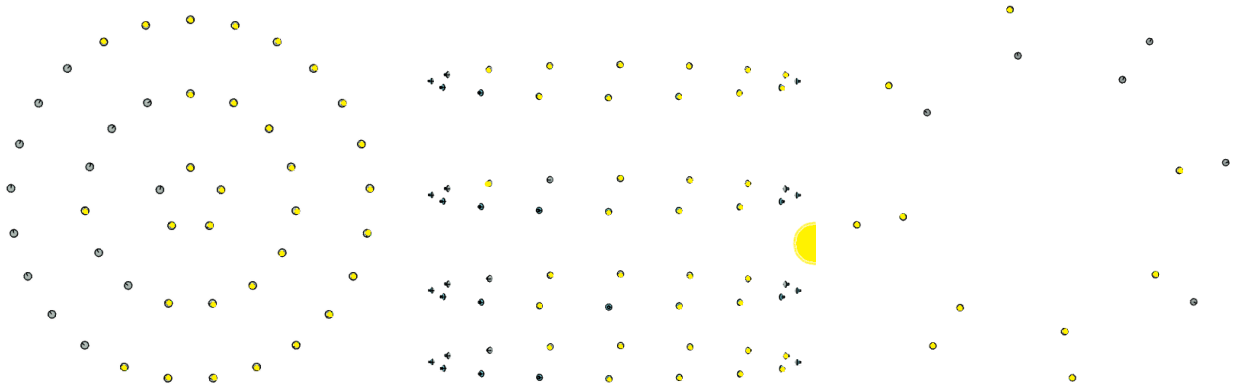

(a) Floor **(b)** Side **(c)** Top

Figure 4.12 – The PMTs highlighted in yellow can be calibrated using the diffuser ball located at coordinates [0, 6000, -1721] mm.

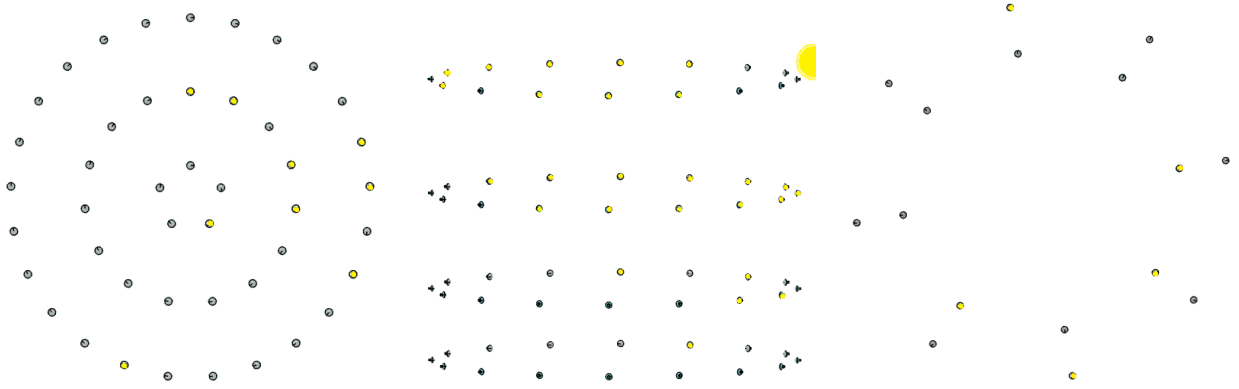

(a) Floor **(b)** Side **(c)** Top

Figure 4.13 – The PMTs highlighted in yellow can be calibrated using the diffuser ball located at coordinates [0, 6000, 3082] mm.

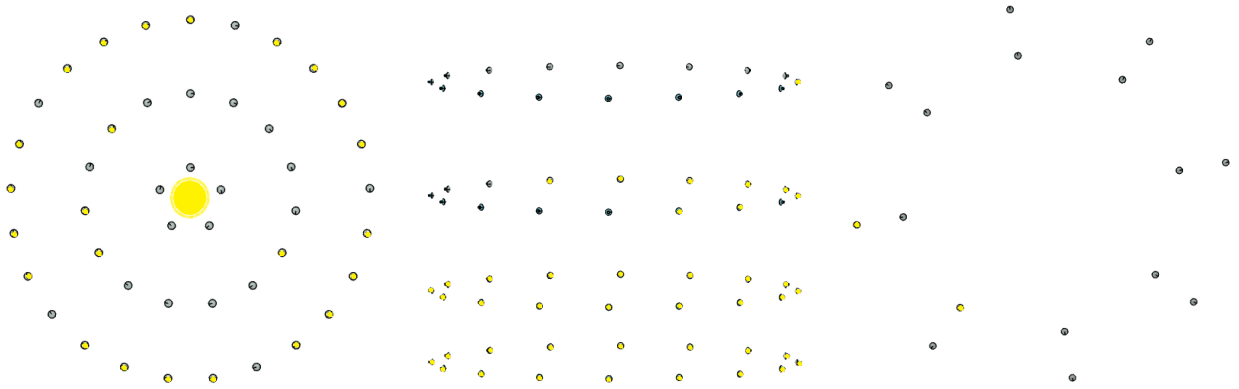

(a) Floor **(b)** Side **(c)** Top

Figure 4.14 – The PMTs highlighted in yellow can be calibrated using the diffuser ball located at coordinates [0, 0, -7038] mm.

Chapter 5

Summary, Conclusion and Future Work

To address a fundamental question in physics — why our world predominantly consists of matter — one avenue of exploration focuses on neutrinos, specifically, we probe whether neutrinos are Majorana particles. They might possess a unique property — being their own antiparticles. The concept of Majorana neutrinos holds significance due to its connection to a theoretical process called "leptogenesis". This process involves violating a conservation law and potentially played a role in generating the observed matter-antimatter imbalance in our universe.

The nEXO experiment, utilizing 5 tonnes of liquid xenon with a 90% enrichment in ^{136}Xe, aimes at advancing our understanding of the neutrino's nature. The considerable amount of xenon employed in this experiment yields a projected sensitivity level of 10^{28} years at the 90% confidence level after ten years of data taking. Particularly noteworthy is the design of the nEXO experiment to facilitate the observation of whether this decay mode exists with a half-life shorter than the projected sensitivity.

To safeguard the decay process from interference by background radiation, a comprehensive approach is employed involving multiple layers of shielding. The experiment's intended location is SNOLAB, an underground laboratory situated at a depth of two kilometers below the surface. Within this setting, a substantial protective measure is the incorporation of a large water tank measuring 12.3 meters in diameter and 12.8 meters in height. This tank is filled with 1.5 kilotonnes of ultra-pure deionized water and serves as the OD.

The OD assumes a multifaceted role. It not only effectively shields the experiment from gamma radiation from the surrounding rock, but also moderates neutrons. Additionally, the OD is instrumented as a muon veto system. This system detects muons that pass through the water, potentially leading to correlated events within the core of the experiment, the inner detector. To fulfill this latter purpose, the OD is outfitted with an array of 125 PMTs.

A calibration system is under development with the primary aim of calibrating the timing properties of the PMTs readout system and concurrently monitoring the optical characteristics of the water. This calibration mechanism is important in ensuring the accurate and reliable functioning of the muon veto. In the context of designing the calibration system for the nEXO OD, insights were gleaned from a comprehensive review of the calibration systems employed in analogous experiments, particularly those concerning the calibration of their muon veto systems. Drawing from this foundation, a calibration system was devised. A concerted effort was made to maintain a design approach characterized by simplicity. The focus on simplicity serves the purpose of preventing the incorporation of external components into the OD setup and simplifying the maintenance procedures related to the calibration system.

The calibration setup for the nEXO OD entails the integration of a fiber optic system that employs laser technology within the water tank. These light sources are carefully chosen to align with the wavelength at which the PMTs demonstrate their optimal efficiency. Initial investigations suggest that light with wavelengths spanning from 360 to 390 nm offers the most favorable outcomes for the designated PMTs. The placement of fibers within the tank is strategically arranged along its inner surface, capitalizing on the exposure of each light point to multiple PMTs for enhanced visibility. At the end of each fiber, diffusers will be implemented to ensure uniform light dispersion across the entirety of the OD.

The analysis showcasing the application of this system was conducted employing Chroma simulations. The outcomes from this analysis affirm that the integration of five diffuser balls proves to be sufficient. Specifically, placing one diffuser on the floor and distributing two each on the right and left walls emerges as an optimal configuration. This configuration optimally addresses the requirements of the calibration setup.

While our simulations have provided valuable insights, the realization of a prototype is a next step to affirm the viability of the calibration system within the actual setup. This bridging of simulation and practical verification is integral in fostering confidence in the calibration system's performance and its seamless integration into the broader experimental framework. Additionally, it is crucial to verify the compatibility of the calibration system with our PMTs through practical experimentation.

Bibliography

[1] James S Trefil. *The moment of creation: Big Bang physics from before the first millisecond to the present universe*. Courier Corporation, 2013.

[2] Klaus Fredenhagen. On the existence of antiparticles. *Communications in Mathematical Physics*, 79:141–151, 1981.

[3] Michio Kaku and Jennifer Trainer Thompson. *Beyond Einstein: The cosmic quest for the theory of the universe*. OUP Oxford, 1997.

[4] Anthony Zee. *Quantum field theory in a nutshell*, volume 7. Princeton University Press, 2010.

[5] Karsten M Heeger. Evidence for neutrino mass: A decade of discovery. In *SEESAW 25*, pages 65–80. World Scientific, 2005.

[6] Andrea Taroni. Nobel prize 2015: Kajita and Mcdonald. *Nature Physics*, 11(11):891–891, 2015.

[7] David Griffiths. *Introduction to elementary particles*. John Wiley & Sons, 2020.

[8] Susanne Mertens. Direct neutrino mass experiments. In *Journal of Physics: Conference Series*, volume 718, page 022013. IOP Publishing, 2016.

[9] Vernon Barger, Danny Marfatia, and Kerry Whisnant. *The physics of neutrinos*. Princeton University Press, 2012.

[10] Frank Close. *Neutrino*. Oxford University Press, 2012.

[11] M Sajjad Athar, Steven W Barwick, Thomas Brunner, Jun Cao, Mikhail Danilov, Kunio Inoue, Takaaki Kajita, Marek Kowalski, Manfred Lindner, Kenneth R Long, et al. Status and perspectives of neutrino physics. *Progress in Particle and Nuclear Physics*, 124:103947, 2022.

[12] K Nakamura, ST Petcov, et al. Neutrino masses, mixing, and oscillations. *Physical Review D*, 98(3):251–286, 2018.

[13] M Magg and Ch Wetterich. Neutrino mass problem and gauge hierarchy. *Physical Letters B*, 94(CERN-TH-2829):61–64, 1980.

[14] Paul Langacker. *The Standard Model and Beyond*. Taylor & Francis, 2017.

[15] Laurie M Brown. The idea of the neutrino. *Physics today*, 31(9):23, 1978.

[16] K Zuber. Double beta decay. *Contemporary Physics*, 45(6):491–502, 2004.

[17] Lothar Oberauer, Aldo Ianni, and Aldo Serenelli. *Solar neutrino physics: the interplay between particle physics and astronomy*. John Wiley & Sons, 2020.

[18] Klaus Grotz and Hans Volker Klapdor. *The weak interaction in nuclear, particle and astrophysics*. CRC Press, 1990.

[19] DR Artusa, FT Avignone, O Azzolini, M Balata, TI Banks, G Bari, J Beeman, Fabio Bellini, A Bersani, M Biassoni, et al. Exploring the neutrinoless double beta decay in the inverted neutrino hierarchy with bolometric detectors. *The European Physical Journal C*, 74:1–19, 2014.

[20] A Giuliani, JJ Cadenas, S Pascoli, E Previtali, R Saakyan, K Schäffner, and S Schoenert. Double beta decay APPEC committee report. *arXiv preprint arXiv:1910.04688*, 2019.

[21] Werner Rodejohann. Neutrinoless double beta decay and particle physics. *International Journal of Modern Physics E*, 20(09):1833–1930, 2011.

[22] A Staudt, K Muto, and HV Klapdor-Kleingrothaus. Calculation of 2ν and 0ν double beta decay rates. *Europhysics Letters*, 13(1):31, 1990.

[23] Petr Vogel. Neutrinoless double beta decay. In *Intersections of Particle and Nuclear Physics (AIP Conference Proceedings Volume 870)*, volume 870, pages 124–131, 2006.

[24] Joseph Schechter and José WF Valle. Neutrinoless double-β decay in SU (2) $\times$ U (1) theories. *Physical Review D*, 25(11):2951, 1982.

[25] SM Bilenky and C Giunti. Neutrinoless double beta decay: a probe of physics beyond the Standard Model. *International Journal of Modern Physics A*, 30:1530001, 2015.

[26] Claudia Patrignani, K Agashe, G Aielli, C Amsler, M Antonelli, DM Asner, H Baer, Sw Banerjee, RM Barnett, T Basaglia, et al. Review of particle physics. 2016.

[27] H Akimune, H Ejiri, F Hattori, C Agodi, M Alanssari, F Cappuzzello, D Carbone, M Cavallaro, G Colo, F Diel, et al. Spin-dipole nuclear matrix element for the double beta decay of ^{76}Ge by the (^{3}He, t) charge-exchange reaction. *Journal of Physics G: Nuclear and Particle Physics*, 47(5):05LT01, 2020.

[28] Ziro Maki, Masami Nakagawa, and Shoichi Sakata. Remarks on the unified model of elementary particles. *Progress of Theoretical Physics*, 28(5):870–880, 1962.

[29] Jose Bernabeu. On the history of the PMNS Matrix... with today's perspective. *arXiv preprint arXiv:1312.7451*, 2013.

[30] N Ackerman, B Aharmim, M Auger, DJ Auty, PS Barbeau, K Barry, L Bartoszek, E Beauchamp, V Belov, C Benitez-Medina, et al. Observation of two-neutrino double beta decay in ^{136}Xe with the EXO-200 detector. *Physical Review Letters*, 107(21):212501, 2011.

[31] Russell Geoffrey Neilson. *Discovery of the Two-neutrino Double Beta Decay of Xenon-136 with EXO-200*. PhD thesis, Stanford University, 2011.

[32] Benjamin JP Jones. The physics of neutrinoless double beta decay: A primer. *arXiv preprint arXiv:2108.09364*, 2021.

[33] JB Albert, M Auger, DJ Auty, PS Barbeau, E Beauchamp, D Beck, V Belov, C Benitez-Medina, J Bonatt, M Breidenbach, et al. Improved measurement of the $2\nu\beta\beta$ half-life of ^{136}Xe with the EXO-200 detector. *Physical Review C*, 89(1):015502, 2014.

[34] Craig Steven Levin. *Sensitivity of a highly compressed xenon gas ionization chamber to the neutrinoless double beta decay of xenon-136*. Yale University, 1993.

[35] D Akimov, G Bower, M Breidenbach, R Conley, E Conti, M Danilov, R DeVoe, Z Djurcic, A Dolgolenko, W Fairbank Jr, et al. EXO: an advanced Enriched Xenon double beta decay Observatory. *Nuclear Physics B-Proceedings Supplements*, 138:224–226, 2005.

[36] N Ishida, M Chen, T Doke, K Hasuike, A Hitachi, M Gaudreau, M Kase, Y Kawada, J Kikuchi, T Komiyama, et al. Attenuation length measurements of scintillation light

in liquid rare gases and their mixtures using an improved reflection suppresser. *Nuclear Instruments and Methods in Physics Research Section A: Accelerators, Spectrometers, Detectors and Associated Equipment*, 384(2-3):380–386, 1997.

[37] M Szydagis, N Barry, K Kazkaz, J Mock, D Stolp, M Sweany, M Tripathi, S Uvarov, N Walsh, and M Woods. NEST: a comprehensive model for scintillation yield in liquid xenon. *Journal of Instrumentation*, 6(10):P10002, 2011.

[38] F Granena, T Lux, F Nova, J Rico, F Sanchez, DR Nygren, JAS Barata, FIGM Borges, CAN Conde, THVT Dias, et al. NEXT, a HPGXe TPC for neutrinoless double beta decay searches. *arXiv preprint arXiv:0907.4054*, 2009.

[39] Yuehuan Wei, Jianyu Long, Francesco Lombardi, Zhiheng Jiang, Jingqiang Ye, and Kaixuan Ni. Development and performance of a sealed liquid xenon time projection chamber. *Journal of Instrumentation*, 16(01):P01018, 2021.

[40] Hans Jurgen Hilke. Time Projection Chambers. *Reports on Progress in Physics*, 73(11):116201, 2010.

[41] E Conti, R DeVoe, G Gratta, T Koffas, S Waldman, J Wodin, D Akimov, G Bower, M Breidenbach, R Conley, et al. Correlated fluctuations between luminescence and ionization in liquid xenon. *Physical Review B*, 68(5):054201, 2003.

[42] S Al Kharusi. *A water Cherenkov muon veto for the nEXO neutrinoless double beta decay experiment*. Thesis to be submitted in 2023.

[43] T. Daniels. Recent Results from EXO-200. *Physics Procedia*, 61:221–222, 2015.

[44] M Auger, DJ Auty, PS Barbeau, L Bartoszek, E Baussan, E Beauchamp, C Benitez-Medina, M Breidenbach, D Chauhan, B Cleveland, et al. The EXO-200 detector, part I: detector design and construction. *Journal of Instrumentation*, 7(05):P05010, 2012.

[45] JB Albert, G Anton, I Badhrees, PS Barbeau, R Bayerlein, D Beck, V Belov, M Breidenbach, T Brunner, GF Cao, et al. Search for neutrinoless double beta decay with the upgraded EXO-200 detector. *Physical review letters*, 120(7):072701, 2018.

[46] G. Anton, I. Badhrees, P. S. Barbeau, D. Beck, V. Belov, T. Bhatta, M. Breidenbach, T. Brunner, G. F. Cao, W. R. Cen, et al. Search for Neutrinoless Double-β Decay with the Complete EXO-200 Dataset. *Physical Review Letters*, 123:161802, Oct 2019.

[47] G Adhikari, S Al Kharusi, E Angelico, G Anton, IJ Arnquist, I Badhrees, J Bane, V Belov, EP Bernard, T Bhatta, et al. nEXO: neutrinoless double beta decay search beyond 10^{28} year half-life sensitivity. *Journal of Physics G: Nuclear and Particle Physics*, 49(1):015104, 2021.

[48] JB Albert, G Anton, IJ Arnquist, I Badhrees, P Barbeau, D Beck, V Belov, F Bourque, JP Brodsky, E Brown, et al. Sensitivity and discovery potential of the proposed nEXO experiment to neutrinoless double-β decay. *Physical Review C*, 97(6):065503, 2018.

[49] S Al Kharusi, A Alamre, JB Albert, M Alfaris, G Anton, IJ Arnquist, I Badhrees, PS Barbeau, D Beck, V Belov, et al. nEXO pre-conceptual design report. *arXiv preprint arXiv:1805.11142*, 2018.

[50] FP An, AB Balantekin, HR Band, W Beriguete, M Bishai, S Blyth, RE Brown, I Butorov, GF Cao, J Cao, et al. The muon system of the Daya Bay Reactor antineutrino experiment. *Nuclear Instruments and Methods in Physics Research Section A: Accelerators, Spectrometers, Detectors and Associated Equipment*, 773:8–20, 2015.

[51] P DeVore, D Escontrias, T Koblesky, CJ Lin, DW Liu, Kam Biu Luk, J Ngan, JC Peng, C Polly, J Roloff, et al. Light-weight flexible magnetic shields for large-aperture photomultiplier tubes. *Nuclear Instruments and Methods in Physics Research Section A: Accelerators, Spectrometers, Detectors and Associated Equipment*, 737:222–228, 2014.

[52] R Alves, S Andringa, S Bradbury, J Carvalho, D Chauhan, K Clark, I Coulter, F Descamps, E Falk, L Gurriana, et al. The calibration system for the photomultiplier array of the SNO+ experiment. *Journal of Instrumentation*, 10(03):P03002, 2015.

[53] J Boger, R.L Hahn, J.K Rowley, A.L Carter, B Hollebone, D Kessler, I Blevis, F Dalnoki-Veress, A DeKok, J Farine, et al. The Sudbury Neutrino Observatory. *Nuclear Instruments and Methods in Physics Research Section A: Accelerators, Spectrometers, Detectors and Associated Equipment*, 449(1-2):172–207, 2000.

[54] BA Moffat, RJ Ford, FA Duncan, K Graham, AL Hallin, CAW Hearns, J Maneira, P Skensved, and DR Grant. Optical calibration hardware for the Sudbury Neutrino Observatory. *Nuclear Instruments and Methods in Physics Research Section A: Accelerators, Spectrometers, Detectors and Associated Equipment*, 554(1-3):255–265, 2005.

[55] Nuno Fiúza de Barros. *Precision measurement of neutrino oscillation parameters: combined three-phase results of the Sudbury Neutrino Observatory*. PhD thesis, Universidade de Lisboa (Portugal), 2011.

[56] James R Sinclair. *Positioning and timing calibration of SNO+*. PhD thesis, University of Sussex, 2015.

[57] V Albanese, R Alves, MR Anderson, S Andringa, L Anselmo, E Arushanova, S Asahi, M Askins, DJ Auty, AR Back, et al. The SNO+ experiment. *Journal of Instrumentation*, 16(08):P08059, 2021.

[58] E Aprile, J Aalbers, F Agostini, M Alfonsi, FD Amaro, M Anthony, B Antunes, F Arneodo, M Balata, P Barrow, et al. The XENON1T dark matter experiment. *The European Physical Journal C*, 77(12):1–23, 2017.

[59] E Aprile, F Agostini, M Alfonsi, K Arisaka, F Arneodo, M Auger, C Balan, P Barrow, L Baudis, B Bauermeister, et al. Conceptual design and simulation of a water Cherenkov muon veto for the XENON1T experiment. *Journal of instrumentation*, 9(11):P11006, 2014.

[60] Arianna Rocchetti. MonteCarlo simulation of the XENON1T experiment and first comparison with the Muon Veto data. Master's thesis, Alma Mater Studiorum - Università di Bologna, 2017.

[61] DS Akerib, CW Akerlof, D Yu Akimov, SK Alsum, HM Araújo, X Bai, AJ Bailey, J Balajthy, S Balashov, MJ Barry, et al. LUX-ZEPLIN (LZ) conceptual design report. *arXiv preprint arXiv:1509.02910*, 2015.

[62] W Turner, A Baxter, HJ Birch, B Boxer, S Burdin, E Fraser, A Greenall, S Powell, and P Sutcliffe. Optical calibration system for the LUX-ZEPLIN (LZ) outer detector. *Nuclear Instruments and Methods in Physics Research Section A: Accelerators, Spectrometers, Detectors and Associated Equipment*, 1010:165551, 2021.

[63] B. J. Mount, S. Hans, R. Rosero, M. Yeh, C. Chan, R. J. Gaitskell, D. Q. Huang, J. Makkinje, D. C. Malling, M. Pangilinan, et al. LUX-ZEPLIN (LZ) Technical Design Report. *arXiv preprint arXiv:1703.09144*, 2017.

[64] K-H Ackermann, M Agostini, M Allardt, M Altmann, E Andreotti, AM Bakalyarov, M Balata, I Barabanov, M Barnabé Heider, N Barros, et al. The GERDA experiment for the search of $0\nu\beta\beta$ decay in ^{76}Ge. *The European Physical Journal C*, 73:1–29, 2013.

[65] M Knapp, P Grabmayr, J Jochum, B Lubsandorzhiev, G Meierhofer, F Ritter, and B Shaibonov. The GERDA muon veto Cherenkov detector. *Nuclear Instruments and Methods in Physics Research Section A: Accelerators, Spectrometers, Detectors and Associated Equipment*, 610(1):280–282, 2009.

[66] Florian Ritter, Bayarto Lubsandorzhiev, Kai Freund, Peter Grabmayr, Josef Jochum, Markus Knapp, Georg Meierhofer, and Bator Shaibonov. The calibration system of the GERDA muon veto Cherenkov detector. *Nuclear Instruments and Methods in Physics Research Section A: Accelerators, Spectrometers, Detectors and Associated Equipment*, 617(1-3):420–421, 2010.

[67] Stanley Reid Seibert and Anthony Latorre. Fast Optical Monte Carlo Simulation With Surface-Based Geometries Using Chroma. *Semantic Scholar*, 2011.

[68] FP An, JZ Bai, AB Balantekin, HR Band, D Beavis, W Beriguete, M Bishai, S Blyth, RL Brown, I Butorov, et al. The detector system of the Daya Bay reactor neutrino experiment. *Nuclear Instruments and Methods in Physics Research Section A: Accelerators, Spectrometers, Detectors and Associated Equipment*, 811:133–161, 2016.

[69] Large Photocathode Area Photomultiplier Tubes. `https://www.hamamatsu.com/jp/en/\product/optical-sensors/pmt/pmt_tube-alone/head-on-type/R5912.html`, Visited August 2023.

[70] JD Jackson. Classical Electrodynamics 3rd ed. New York: John Wiley&Sons, 1999.

[71] Permeability. `https://en.wikipedia.org/wiki/Permeability_(electromagnetism)`, Visited August 2023.

[72] Refractive index database. `https://refractiveindex.info/?shelf=main&book=H2O&page=Hale`, Visited August 2023.

[73] Harvey J Hindin. Wolfram Alpha. *Mathematics and Computer Education*, 44(1):77, 2010.

[74] Leif Rädel and Christopher Wiebusch. Calculation of the Cherenkov light yield from low energetic secondary particles accompanying high-energy muons in ice and water with Geant4 simulations. *Astroparticle Physics*, 38:53–67, 2012.

[75] PHOTOMULTIPLIER TUBES, Basics and Applications, 4th edition. `https://www.hamamatsu.com/content/dam/hamamatsu-photonics/sites/documents/99_SALES_LIBRARY/etd/PMT_handbook_v4E.pdf`, Visited August 2023.

[76] JHM Hakvoort and M Donze. The optical properties of pure water H. Buiteveld Institute for Inland Water Management and Waste Water Treatment, Ministry of Transport and Public Works, PO Box 17, 8200 AA Lelystad, The Netherlands.

[77] S. Agostinelli, J. Allison, K. Amako, J. Apostolakis, H. Araujo, P. Arce, M. Asai, D. Axen, S. Banerjee, G. Barrand, et al. GEANT4—a simulation toolkit. *Nuclear instruments and methods in physics research section A: Accelerators, Spectrometers, Detectors and Associated Equipment*, 506(3):250–303, 2003.

[78] Bjarne Stroustrup. An overview of the C++ programming language. *Handbook of object technology*, page 72, 1999.